

Defects and their Time Scales in Quantum and Classical Annealing of the Two-Dimensional Ising Model

Phillip Weinberg,^{1,2,*} Na Xu,^{1,†} and Anders W. Sandvik^{1,3,‡}

¹*Department of Physics, Boston University, 590 Commonwealth Avenue, Boston, Massachusetts 02215, USA*

²*Department of Physics, Northeastern University, Boston, Massachusetts 02115, USA*

³*School of Physical and Mathematical Sciences, Nanyang Technological University, Singapore*

(Dated: July 15, 2025)

We investigate system-size and ramp-velocity scaling of defects remaining in the two-dimensional transverse-field Ising ferromagnet on periodic $L \times L$ lattices after quantum annealing from high to vanishing field. Though the system sizes that we can study using exact integration of the Schrödinger equation are limited to $L \leq 6$, we clearly observe the critical Kibble-Zurek (KZ) time scale $\propto L^{z+1/\nu}$ (with 3D Ising exponents, $z = 1$ and $\nu \approx 0.63$) at the quantum phase transition. We also observe KZ scaling of the gap-protected ground-state fidelity at the end of the process. Other quantities in the ordered phase depend on excited states evolving by coarsening dynamics of confined defects, with a time scale $\propto L^2$, and interface fluctuations of system-spanning stripe defects with life time scaling as L^3 . Some of our methods and conclusions build on analogies with classical simulated annealing, for which we also obtain new insights. We characterize in detail the evolution of system-spanning domains—topological defects characterized by winding numbers in periodic systems—and find differences in the dynamic scales of domains with winding numbers $W = (1, 0)/(0, 1)$ (those spanning the system only horizontally or vertically) and $W = (1, 1)$ (spanning the system diagonally). The former decay on a time scale $\propto L^3$ in the ordered state at fixed temperature while the latter exhibits a longer scale $\propto L^{3.4}$. As a consequence of $L^{3.4}$ exceeding the classical KZ scale $L^{z+1/\nu}$ with $\nu = 1$ and $z \approx 2.17$, the probability of the system hosting $W = (1, 1)$ domains scales with the KZ exponent even when observed in the final $T = 0$ state, where conventional observables are governed by the L^2 and L^3 ordering time scales. We observe the same time scales in systems with open boundary conditions, except for the lack of the slower time scale of diagonal domain walls, which in this case smoothly evolve to horizontal or vertical walls. In QA, the L^3 time scale for elimination of $W = (1, 0)/(0, 1)$ domains through interface fluctuations also exceeds the relevant KZ scale and the KZ mechanism is therefore responsible for elimination of these domains. The L^3 scale can nevertheless be detected in the collective evolution of the excited states, using a method of analysis that we develop for this purpose and which should also be applicable in QA experiments. The presence of three different time scales at the end of the protocol offers opportunities for rigorous multifaceted tests of QA devices with the methods developed here.

I. INTRODUCTION

The metallurgical method of annealing a crystalline solid to reduce its density of defects has lent its name to the metaheuristic optimization algorithms of simulated annealing (SA) [1–3] and quantum annealing (QA) [4–8]. In SA, a Monte Carlo (MC) simulation of a model whose ground state represents a hard optimization problem, e.g., the paradigmatic Ising spin glass, is performed with a gradually lowered temperature, eventually freezing the system into a low-energy state [1, 9, 10]. In contrast to this classical computational scheme, QA is envisioned as a potentially more powerful optimization method when implemented as a physical device, in which quantum fluctuations of coupled qubits are regulated at very low temperature with the aim of reaching the same classical ground states as in SA. Promising programmable devices suitable for QA experiments include arrays of superconducting qubits [11–20] and Rydberg atoms [21–25]. Our

work reported here is in a large part motivated by the need to quantitatively understand the ground-state convergence of QA processes in these systems. To this end, we will also study SA, which in some respects provides a useful analogy to QA though also differing from QA in crucial ways that we will elucidate here.

A main focus on experimental QA has been to observe Kibble-Zurek (KZ) [26, 27] scaling—the build-up of critical fluctuations in the neighborhood of a continuous quantum phase transition [28–30] as the annealing time is increased. For an annealing process starting from a disordered state and ending in an ordered phase (conventional, “glassy”, or topological) a phase transition must be traversed. In the case of a transition that is continuous in equilibrium, the interplay of the KZ mechanism and other ordering processes [34, 35] poses a challenging out-of-equilibrium many-body problem, in QA as well as in SA [36–41] (and similar phenomena arise also when annealing through a weak first-order transition [42, 43]). Given the increasing experimental attention and capability to detect production of different defects and their time scales [16, 24, 25, 44], further theoretical and computational studies of nonequilibrium criticality and ordering kinetics are called for. We here consider the prototypi-

* Present address: QuEra, Cambridge, Massachusetts, USA

† Present address: Amazon, Seattle, Washington, USA

‡ Communicating author: sandvik@bu.edu

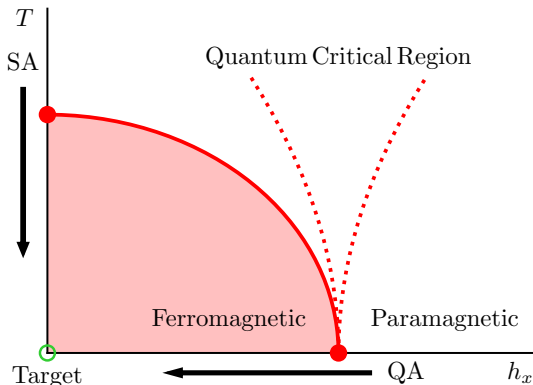


FIG. 1. Phase diagram of the 2D TFIM in the plane of temperature (T) and transverse field (Γ). The two arrows represent the annealing paths taken here in QA and SA processes. The green circle indicates the target classical ground state. While the quantum-critical $T > 0$ regime is not traversed with the paths taken here, a finite QA velocity has effects similar to $T > 0$, with energy pumped into the system in the neighborhood of the critical point and the excitations subsequently thermalizing.

cal example of the two-dimensional (2D) Ising model by numerical SA and QA, systematically investigating the ordering dynamics in terms of both the growth of critical fluctuations close to the phase transition and the subsequent formation of long-range order through other mechanisms.

Figure 1 shows a schematic phase diagram of the 2D $S = 1/2$ transverse-field Ising model (TFIM) that we will study under both QA and SA. The Hamiltonian is

$$H = -J \sum_{\langle ij \rangle} \sigma_i^z \sigma_j^z - \Gamma \sum_{i=1}^N \sigma_i^x, \quad (1)$$

where σ_i^z and σ_i^x are the standard Pauli matrices, $\langle ij \rangle$ refers to nearest neighbors on the 2D square lattice, and $J, \Gamma \geq 0$. In principle, any path in the plane of temperature and coupling ratio Γ/J can be taken when annealing to the classical ground state at $T = 0$, $\Gamma = 0$. Here we will consider the two limiting cases of pure SA and pure QA, as illustrated in Fig. 1. In SA we set the field strength to $\Gamma = 0$ and use MC simulations with local single-spin updates to anneal the classical system versus the temperature T from far above the transition temperature to $T = 0$. In QA, using exact numerical integration of the Schrödinger equation for small systems, we start from the ground state at $J = 0, \Gamma = 1$ and change the couplings versus time such that $J \rightarrow 1$ and $\Gamma \rightarrow 0$ at the end of the process. In either case, the equilibrium phase transition (emerging in the limit of infinite system size) is continuous and critical fluctuations can be observed in the neighborhood of the transition temperature T_c (in SA) or coupling ratio $(\Gamma/J)_c$ (in QA) even if the process is not completely adiabatic (in QA) or quasi-static (in SA). However, the associated KZ scaling is only one of

the interesting aspects of the annealing processes, with the subsequent stage of reaching deep into the ordered phase presenting additional complexity.

Though the Ising ferromagnetic ground state is trivial, there are still open issues regarding the efficiency of QA and SA processes to reach it as a function of the system size and the annealing time. Even though our numerical simulations of QA reach only up to 6×6 spins, we still observe remarkably good scaling behaviors with no less than three distinct time scales as $\Gamma \rightarrow 0$, related to criticality (the KZ mechanism) as well as the kinetic processes leading to the ordered phase by coarsening of confined domains and slow fluctuations of system-spanning domain walls. Many of our methods of data analysis and interpretations of results for QA are guided by analogies with SA, which we study first using large lattices (L up to several hundred). In particular, we obtain new qualitative and quantitative insights into the development and persistence of system-spanning topological defects. This aspect of our work also relates more broadly to generic questions about the stability of large-scale defects in quantum and classical many-body systems out of equilibrium, with the 2D Ising models serving as paradigmatic examples for which reliable numerical results can be obtained—in the quantum case perhaps surprisingly, given that we only study systems with up to 36 spins.

In QA, we study not only physical observables in terms of their conventional expectation values, but also develop a scheme to isolate the evolution of the excited states from the dominant ground state at long annealing times—a method that can also be implemented experimentally. Our work firmly establishes the 2D Ising model as a non-trivial system for multifaceted tests of experimental QA devices. Moreover, we propose specific QA experiment that may provide further insights into emergent collective ordering kinetics beyond what can be derived from the small systems studied here. Our study can also serve as a benchmark for more sophisticated but approximative numerical solutions of the Schrödinger equation, which so far have not been able to study ordering kinetics of the 2D TFIM and related models at the level achieved here. Though much larger systems were simulated in some of the past studies [18, 45–47], they were limited by the break-down of assumptions and accumulation of integration errors to very short annealing times, corresponding to only to the initial stages of ordering.

Below we give a brief synopsis the main issues addressed and the key results obtained. The KZ scaling and defect “evaporation” aspects of the study are summarized in Secs. IA and IB, respectively, and the organization of the rest of the paper is outlined in Sec. IC.

A. Kibble-Zurek scaling

The first interesting stage of a QA or SA process is when the control parameter traverses its critical value. The way the finite annealing rate affects critical scal-

ing properties can be understood in terms of an ansatz originating in early works by Kibble [26] and Zurek [27] on topological defects. The originally classical KZ ideas were later generalized to quantum systems [28–30] and further developed for different annealing protocols and methods of analysis [31–33, 37–39, 48–57]. KZ scaling behaviors follow from the relationship between the correlation length ξ and the relaxation time τ , which at a conventional classical or quantum phase transition is $\tau \propto \xi^z$, where z is the dynamic exponent and ξ diverges as $\delta^{-\nu}$ when the distance δ to a critical point is taken to zero; in our cases, Fig. 1, $\delta = T - T_c$ when $\Gamma = 0$ and $\delta = \Gamma - \Gamma_c$ when $T = 0$ (and we neglect any minus sign, treating δ as $|\delta|$). In terms of the rate (velocity) v by which the relevant parameter is changed when passing through the critical point, the divergence of the correlation length is cut off at a velocity dependent maximum value,

$$\xi_v \propto v^{-\nu/(z\nu+1)}, \quad (2)$$

which is attained when the annealing parameter is close to its critical value and v is sufficiently small.

In QA, z is the intrinsic dynamic exponent, i.e., $z = 1$ in the TFIM, while in SA it corresponds to the stochastic process applied, e.g., $z \approx 2.17$ for local MC updates (e.g., Glauber dynamics with single-spin flips used here) in the classical 2D Ising model [53, 58]. Velocity-limited critical forms of physical observables $A(\delta)$ in the thermodynamic limit can be obtained from the conventional equilibrium critical expressions by using $\delta \propto \xi^{-1/\nu}$ and then replacing the equilibrium correlation length ξ by its velocity limited form ξ_v in Eq. (2).

The KZ mechanism also implies a power-law relationship between the quasi-static or -adiabatic annealing time and the system size, which provides a useful way to analyze numerical simulation results as well as QA experiments. This is the form in which we will consider KZ scaling here. From Eq. (2), by replacing ξ_v by the system length L , the KZ time scale that has to be attained for the system to remain in equilibrium all the way to the infinite-size critical point ($\delta = 0$) is

$$t_{\text{KZ}} \propto L^{z+1/\nu}. \quad (3)$$

For a generic quantity A with equilibrium critical form $A \propto \delta^\kappa$, with a corresponding generic exponent κ , the velocity and size dependence when the annealing has reached the critical point can be written as

$$A(v, L) = L^{-\kappa/\nu} f(vL^{z+1/\nu}), \quad (4)$$

where the analytic scaling function $f(x)$ takes a constant value for $x \rightarrow 0$ and L has to be sufficiently large for finite-size scaling corrections to be negligible. For large x , the trivial size dependence of A when $\xi_v \ll L$, e.g., L independent or $A \propto L^{-d}$, demands a specific power-law form of $f(x) \sim x^a$ [53] that is easily obtained from Eq. (4) by choosing the exponent a such that $L^{-\kappa/\nu}(vL^{z+1/\nu})^a$

contains the appropriate power of L , thus also producing the velocity dependence.

Our main aim here is to study kinetic processes affecting QA or SA beyond the critical point, eventually as $\Gamma \rightarrow 0$ or $T \rightarrow 0$. In such a process many different quantities can be computed (or measured in experiments) and they can be analyzed in different ways to reveal scaling behaviors. We will see that KZ scaling can be observed in some quantities even at the extreme end ($\Gamma = 0$, $T = 0$) of an annealing process, but in different ways in QA and SA. In QA, the ground state fidelity, i.e., the “success probability” in the context of optimization, is protected by the gap in the ferromagnetic phase and is almost fully locked into its final value as the system passes the quantum-critical point. We indeed observe extremely good KZ scaling of the ground state fidelity at the final $\Gamma = 0$ state of the QA process, despite the system sizes being restricted to $L \leq 6$. Most other physical observables depend in some way on excited states, which are not governed by the KZ mechanism because of the gapless spectrum (for increasing L) above the lowest excited state and the related faster kinetic processes that we will investigate in detail. Likewise, in SA the system annealed deep into the ordered phase is subject to ordering processes unrelated to the critical fluctuations underlying the KZ mechanism. Interestingly, we find that the survival time of certain system-spanning stripe defects still obeys KZ scaling, because these defects are absent below T_c in equilibrium and their elimination by fluctuations (if imposed by hand in an initial state) is governed by a longer time scale than the KZ time required for the system to stay in equilibrium when traversing the critical point.

B. Dynamics in the ordered phase

In early discussions of KZ scaling, the assumption was that the topological defects produced when passing through the critical point would stay essentially frozen when annealing further into an ordered phase. If all dynamical processes in the ordered state are much slower than the KZ rate $v_{\text{KZ}} = 1/t_{\text{KZ}}$, then the near-critical state with correlation length ξ_v in Eq. (2) (assuming $L \gg \xi_v$) remains essentially unchanged all the way to $T = 0$ in SA or in the classical limit of the Hamiltonian in QA. Likewise, a finite system that has stayed in equilibrium all the way to the transition point would remain close to its critical state also when the process continues into the ordered phase. This aspect of QA is of relevance in experiments when the state can be accessed only in the classical limit, e.g., $\Gamma \rightarrow 0$ in D-Wave devices [11]. Indeed, it was possible to demonstrate KZ scaling in D-Wave QA of Ising spin glasses thanks to the slow dynamics of the glassy state [17, 18]. In general, the system of course must always continue to evolve to some extent also beyond the critical point, and, for sufficiently slow annealing, an ordered state (conventional or

glassy) eventually develops through processes beyond the KZ mechanism, by fluctuations facilitating energy minimization. A finite system will reach its true classical ground state this way over an extent of time that scales with the system size. In many cases, some of these kinetic ordering processes are actually faster than the KZ scale and do not rely on a critical state having built up with correlation length $\xi_v \approx L$ first. If all defects can be eliminated faster than the KZ scale, the critical stage with correlation length $\xi_v \approx L$ can be completely bypassed.

The relevant dynamical processes of course depend on the system under study. In the case of the classical uniform Ising model, coarsening dynamics [34, 36] involving confined defects such as those illustrated in Fig. 2(a) involves a faster time scale $t_{\text{coa}} \propto L^2$ to ordering below T_c than the KZ time $t_{\text{KZ}} \propto L^{z+1/\nu}$ required for a finite system to reach its critical state. An annealing time of order L^2 may therefore appear sufficient for the system to reach the ferromagnetic state at $T = 0$ from any initial temperature. When reaching the critical point in such a process, the correlation length is ξ_v , with $v \propto L^{-2}$ in Eq. (2), which grows slower than L (in both SA and QA). Thus, the fully critical finite-size state where $\xi \approx L$ is bypassed. Proceeding into the ordered phase, the fractal critical domains of typical size $\xi_v \ll L$ begin to develop smooth domain boundaries (coarsen) over time. Eventually an ordered state with isolated defects form, as in Fig. 2(a), and the fully ordered state develops when these confined defects shrink away. For $v = \lambda L^{-2}$, with sufficiently small λ , all confined domains are eliminated at the end of the anneal ($T = 0$, $\Gamma = 0$). However, this scenario neglects the possibility that a time scale longer than L^2 may be required to remove topological, system-spanning domains that appear in some annealing instances [36] and are illustrated in Figs. 2(b) and 2(c). As far as we are aware, the processes of final elimination of these system-spanning defects have not been quantitatively studied, neither in QA nor SA of the 2D Ising model, though similar large-scale defects are at the heart of the seminal KZ works [26, 27].

System-spanning defects in the classical 2D Ising model have been studied in other contexts. In instantaneous MC quenches from $T = \infty$ to $T = 0$ [59–62] it was observed that a finite fraction of final states remain with completely straight domain walls (which cannot be removed by single-spin flips at $T = 0$) while diagonally oriented domains can shrink away and do so at a time scale L^a , with the value of the exponent estimated at $a \approx 3.5$. It was also argued that horizontally or vertically oriented domains vanish on a shorter time scale L^3 at low temperature [59, 63]. The apparently different behaviors of these two types of system-spanning domains at $T > 0$ has not been explained quantitatively, though related work suggests non-universal interface diffusivity [64]. Here we will investigate the stochastic-dynamical aspects of system spanning domain walls in SA and obtain further insights into their relevant time scales and how they can be observed. We also carry out extensive

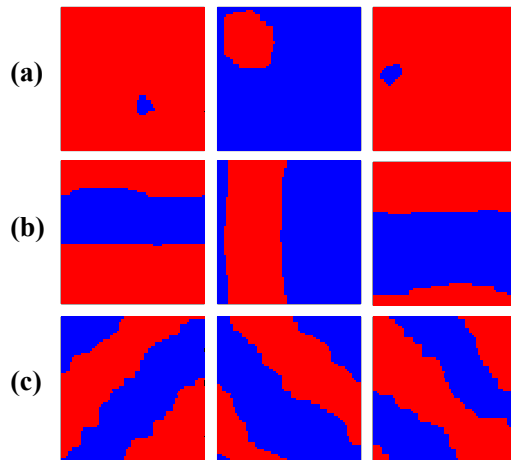


FIG. 2. Spin configurations of a classical $L = 64$ periodic Ising system (up and down spins shown as red and blue squares) with defects remaining after annealing from $T = 4$, above $T_c \approx 2.27$, to $T = 0$ in a linear ramp using a total of 2^{10} MC sweeps (each consisting of L^2 random single-spin flip attempts with Metropolis acceptance probability). The three rows exemplify different types of defects; (a) confined domains with winding number $(0, 0)$, which are formed and eventually vanish (for longer annealing times) through standard coarsening dynamics, (b) system-spanning stripe domains oriented along a system axis, with winding number $(1, 0)$ or $(0, 1)$, and (c) diagonal stripe domains with winding number $(1, 1)$. Note that each of the configurations in (b) and (c) only have two domains because of the periodic boundary conditions. The system spanning domains can vanish through interface fluctuations, when the two domain walls touch each other, thus breaking the stripe and allowing the resulting defect with winding number $(0, 0)$ to shrink as those in (a). The time scale for eliminating winding domains in SA is longer than the coarsening scale L^2 .

studies of the time scales of elimination of horizontal and diagonal system-spanning domains by domain-wall fluctuations at fixed temperatures below T_c . We confirm the L^3 time scale for elimination of domain walls in the case of $W = (1, 0)$ and obtain a more precise value of the exponent for $(1, 1)$ domains; $a = 3.42 \pm 0.02$.

The $W = (1, 1)$ diagonal domains are particularly interesting, as their probability of survival in an SA process crossing the critical temperature obeys KZ scaling even in the final $T \rightarrow 0$ state, because of their longer time scale of vanishing through domain-wall diffusion below T_c . While diagonal domains are present in equilibrium only close to T_c (in a window of size scaling as $L^{-1/\nu}$, as we will also show explicitly) in SA they are present also below T_c with a probability set by KZ scaling, with their decay taking place primarily very close to T_c . Their overall impact on most physical observables is minor, however, and only the L^2 and L^3 scales are clearly visible when $T \rightarrow 0$ in observables such as the order parameter and the excess energy. To observe the KZ scaling of diagonal domains in the ordered phase, the system has to be probed explicitly for this kind of domains, using

the corresponding winding-number probability (in periodic systems) or other quantities that vanish when $T \rightarrow 0$ unless a diagonal domain is present.

We also investigate system-spanning domain walls on lattices with open boundary conditions, for which the winding number cannot be defined. Indeed, in this case we find that an imposed diagonal domain wall (between opposite corners) decays away on the coarsening time scale L^2 , either resulting in a fully ordered state or, as an intermediate step (the final step if $T = 0$), first evolving into a horizontal or vertical domain wall. In the latter case, we find a logarithmic (log) correction to the L^2 scaling, and the time to final elimination of the remaining system-spanning domain wall is still of order L^3 , which is reflected in physical observables in the same way as in the periodic systems.

In QA of the TFIM, the defects and their time scales inside the ordered state have been less studied than their classical counterparts. There is evidence to suggest that QA of a system described by a generic non-integrable Hamiltonian is governed by classical hydrodynamic behavior deep inside an ordered phase, as a consequence of the system thermalizing with the excess energy acquired when passing the phase transition [38, 65, 66]. A competing theory asserts that the defect production is determined simply by Landau-Zener (LZ) transitions between a few low energy eigenstates near the critical point [29, 67–72]. To our knowledge, the LZ scaling argument has only been tested on integrable 1D models or in mean-field theories, however. The correct description of the defect dynamics in the ordered phase in integrable models follows from an extensive number of conserved quantities, which leads to the break-down of classical hydrodynamics. Regardless of details, these dynamic processes may again possibly be faster than the critical KZ dynamics. In the 1D TFIM, the KZ and LZ exponents are in fact identical, which makes it more difficult (though not impossible) to distinguish the two mechanisms [15, 72].

In the specific case of the 2D TFIM considered here, a recent numerical study based on time evolved matrix- and tensor-product states [45] was not able to reach far inside the ordered phase, but a generalized KZ mechanism was argued to describe the available near-critical data, and signs of quantum coarsening were observed further inside the ordered phase. However, the coarsening time scale was not determined. Though recent progress has been made on more efficient numerical algorithms [46, 47], in general it is still very difficult to solve the Schrödinger equation on size and time scale now accessible in 2D and 3D QA experiments [17, 18, 24].

In our exact numerical solutions of TFIMs with $L \leq 6$, there is no limitation on the duration of the QA process. Even though the systems are very small compared to those used in the classical SA studies, and even in the recent study of QA with matrix- and tensor-product states [45], we find that QA is perfectly consistent with coarsening dynamics with the same time scale as in the classical SA case; $t_{\text{coa}} \propto L^2$. This time is again shorter than the

KZ time scale $t_{\text{KZ}} \propto L^{z+1/\nu}$, now with the 3D Ising exponents $z = 1$ and $\nu \approx 0.63$. Thus, the system can order by coarsening, and KZ scaling can in general not be observed after the annealing parameter has reached deep into the ordered phase. A notable exception is the ground state fidelity (“success probability”), which is protected by the gap in the ferromagnetic phase and is almost fully locked into its final value as the system passes the quantum-critical point. We indeed observe extremely good KZ scaling of the ground state fidelity at the final $\Gamma = 0$ state of the QA process. Some perturbed form of KZ scaling still likely applies very close to the critical point [17, 41, 45], but we find that the fast L^2 coarsening time dominates the behavior far inside the ordered phase as the excited states are not gap-protected and appear to develop essentially classical dynamics. This behavior is consistent with the generic scenario of thermalization of excitations in the ordered phase [38, 65, 66] but has not been observed previously with reliable numerics of the prototypical TFIM.

The fate of system-spanning stripe domains has not been addressed specifically in the context of QA (e.g., in Ref. 45), but, because of the plausible emergence of classical dynamics of a thermalized state, we would expect them to behave much as in SA in the ordered phase. We will show that $W = (1,0)/(0,1)$ domains can be studied quantitatively even in very small systems and their time scale of elimination in QA is indeed L^3 , as in the classical case. However, this time scale is longer than the quantum KZ scale $L^{2.59}$ (unlike SA, in which the KZ scale $L^{3.17}$ exceeds L^3) and its presence in the data is more subtle. We develop a method to study the collective QA evolution of the excited states, where we detect both the L^2 and L^3 time scales. The system sizes are too small to accommodate proper $W = (1,1)$ domains, and we therefore cannot analyze those specifically in QA.

C. Outline and calculation strategy

Given that we will use insights from SA to understand novel aspects of QA in the ordered state of the TFIM, we begin in Sec. II by exploring the final-stage $T \rightarrow 0$ ordering kinetics of the 2D Ising model subject to classical SA. Finite-size KZ scaling in SA of the Ising model has been extensively studied in the past [53] and will only be considered here in our analysis of system-spanning domain walls. In Sec. IIA we first study physical observables, the order parameter and the excess energy, in systems after annealing to $T = 0$, detecting the L^2 coarsening scale and the L^3 scale of elimination of $W = (1,0)/(0,1)$ stripe domains. In Sec. IIB we study the time scales of elimination of $W = (1,0)$ and $W = (1,1)$ domains at fixed $T < T_c$. We return to SA in Sec. IIC to quantify how system-spanning domains form and vanish during the SA process, using winding probabilities as a quantitative measure of the different types of system-spanning defects. All the above simulations are done with periodic

boundary conditions. In Sec. IID we investigate systems with open boundaries.

Turning to QA of the TFIM, in Sec. III we perform exact numerical integration of the Schrödinger equation for systems with up to 6×6 spins and use the insights from SA to analyze the results. In Sec. IIIB we first confirm KZ scaling both at the infinite-size quantum-critical point and, in the case of the fidelity, also at the classical end point of the QA process. In Sec. IIIA we analyze other physical observables in the ordered phase, extracting the dominant coarsening time scale L^2 as well as the L^3 scale we find and associate with the removal of remaining straight domain walls. In Sec. IV we conclude with further discussion of our findings and the applicability of the results to QA experiments.

II. CLASSICAL SIMULATED ANNEALING

We here consider the classical 2D Ising ferromagnet described by the Hamiltonian

$$H_{\text{cl}} = -J \sum_{\langle ij \rangle} \sigma_i \sigma_j, \quad \sigma_i = \pm 1, \quad (5)$$

where the coupling is set to $J = 1$ and $\langle ij \rangle$ stands for nearest-neighbor sites on the 2D square lattice with L^2 spins. In most cases, in Secs. II A–II C, we apply periodic boundary conditions but in Sec. IID we also present results for systems with open boundaries, to confirm universality of the SA time scales. We also find some important differences related to system-spanning defects.

We apply SA with single-spin updates (Glauber dynamics) to the system, starting from an equilibrated state at a temperature T_{init} well above the critical temperature $T_c = 2/\ln(1 + \sqrt{2}) \approx 2.27$, continuing all the way down to $T = 0$ following the standard linear protocol

$$T(t) = T_{\text{init}}(1 - t/t_{\text{SA}}). \quad (6)$$

Here the dimensionless time t is an integer representing the number of MC sweeps, with each sweep involving $N = L^2$ flip attempts of randomly selected spins subject to the Metropolis acceptance probability. The temperature is changed after each MC sweep. The number of sweeps of the entire SA process is t_{SA} and we define the annealing velocity v to be the inverse of the total annealing time; $v = 1/t_{\text{SA}}$, i.e., not including the total change of T by T_{init} units.

We have implemented multi-spin coding, where a single 64-bit integer (in some cases 32-bit) represents 64 independent spins; thus each SA realization contributes 64 distinct contributions to the averages of quantities accumulated at the end of each repetition. The total number of repetitions depends on the velocity and the system size, from over 10^8 for small systems to about 10^4 for the most time-consuming cases of low v and large L . Many of the quantities we study are self-averaging, thus reducing the required number of SA repetitions for large systems.

A. Coarsening and large-scale defects

To study scaling of common physical observables in systems after annealing to $T = 0$, we here use lattice sizes from $L = 16$ to $L = 768$ and velocities spanning a wide enough range for observing the evolution of the final state from completely disordered to essentially fully polarized. Fig. 2 shows some examples of spin configurations at the end of SA runs for an $L = 64$ system at velocity $v = 2^{-10}$, which is low enough (for this rather small system) for the final $T = 0$ state to typically contain only a small number of defects with respect to the fully polarized ferromagnet (and no defects in a significant fraction of the instances). The defects can broadly be classified into three different groups represented by the rows of Fig. 2; confined domain walls in row (a), system-spanning domain walls winding across the periodic boundaries only in the x or y direction in (b), and diagonal domain walls winding in both the x and y directions in (c). In these cases each instance hosts a single defect domain, which is typically the case at some point before a system orders perfectly. In the case of the system-spanning stripe defects, they can also wind around the periodic boundaries multiple times, beyond the winding once in one lattice direction in Fig. 2(b) and once in both directions in Fig. 2(c). The higher winding numbers are naturally less prevalent, and we will present some statistics in Sec. II C.

To quantify the effects of remaining defects, at the end of each annealing instance we first study the mean squared order parameter (magnetization),

$$m^2 = \left\langle \left(\frac{1}{N} \sum_{i=1}^N \sigma_i \right)^2 \right\rangle, \quad (7)$$

and the Ising energy density (where we use a subscript z for consistency with the later study of the TFIM)

$$e_z = \langle H_{\text{cl}} \rangle / N, \quad (8)$$

which we will analyze relative to the size-independent equilibrium value $e_{z,0} = -2$ for systems with periodic boundary conditions at $T = 0$.

We will assume v and L scaling forms $L^{-b} f(vL^\alpha)$ for these quantities in analogy with the KZ form Eq. (4) with some exponents α and b . We first present simple arguments for the exponent b for m^2 and e_z : At some point of the process there will be one or a few large defect domains in an essentially ordered background (possibly with some additional small defects that are not important). These large domains are initially of size some significant fraction of the system size, i.e., of typical length $l \propto L$ (regardless of whether these defects are confined or system-spanning). Thus, the deviation of the magnetization density from its maximum value is of order unity and, therefore, $b = 0$ for m^2 . Close to equilibrium, when $T \rightarrow 0$ and m^2 approaches 1, $1 - m^2$ should be analyzed with a different exponent but here we focus on the stage when the large defects are present and gradually shrink

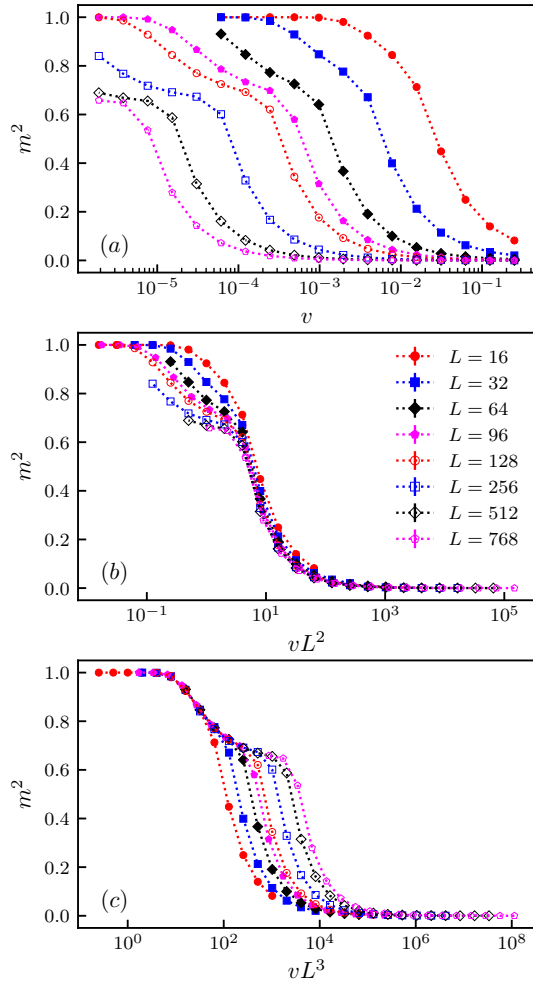


FIG. 3. Squared magnetization averaged over large numbers of SA instances at $T = 0$. (a) Raw data vs the annealing velocity for system sizes $L = 16, 32, 64, 96, 128, 256, 512$, and 768 , according to the legends in panel (b). In (b) and (c), the velocity is rescaled by L^2 and L^3 , respectively, to demonstrate regions of data collapse with two different time scales in the growth of the order parameter.

versus time. In the case of the energy, the total cost of the domain walls is then of order $l \propto L$, which for the excess energy density implies $e_z - e_{z,0} \propto L^{-b}$ with $b = 1$. Thus, to account for both size and velocity dependence, we will test the scaling forms

$$m^2(v, L) = f_m(vL^\alpha), \quad (9a)$$

$$e_z(v, L) = e_{z,0} + \frac{1}{L} f_e(vL^\alpha), \quad (9b)$$

where the exponent α on the time scale L^α will be obtained from numerical data. As we will see, data in different regimes of v and L exhibit scaling with different values of α , i.e., the same SA process can be described by more than one scaling function—at least two in the cases studied here.

Figure 3 summarizes our results for m^2 . The raw data versus v for several different system sizes are shown in

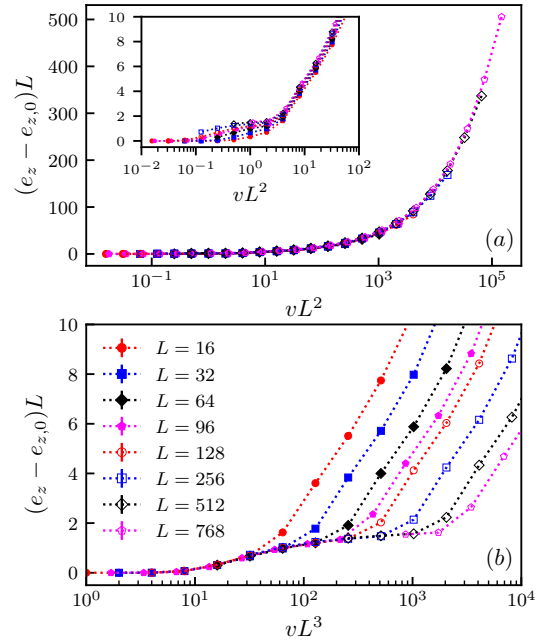


FIG. 4. Excess mean Ising energy density scaled by the system length L at the end of the same SA runs as those in Fig. 3. The data are plotted against vL^2 in panel (a) and vL^3 in panel (b). The legends in (b) apply to the data sets in (a) as well. The inset of panel (a) shows a zoomed-in view of the lower left-hand corner of the main panel.

Fig. 3(a). In addition to an overall shift of the curves toward lower velocity when the system size increases, for the larger systems there is also a qualitative change in behavior before the systems approach the fully polarized state with $m^2 = 1$; the increase is slowed down and a shoulder-like feature forms at $m^2 \approx 0.6$. As shown in Fig. 3(b), by graphing the data versus vL^2 the overall shift with L when m^2 is below the shoulder value is collapsed onto a common curve for the larger system sizes (for which corrections to the leading behavior are small), thus demonstrating a time scale $\propto L^2$ and delivering the corresponding scaling function $f_m(vL^2)$ with $\alpha = 2$ in Eq. (9a). This is the expected well-known time scale of coarsening dynamics [34], which was also studied previously in the context of the $T < T_c$ break-down of KZ scaling in SA of the 2D Ising model [36]. Conventional coarsening here refers to the process by which confined domains, such as those in Fig. 2(a), minimize their boundary energy by tending toward circular smooth shapes that also shrink at low temperatures; eventually vanishing in the case of SA to $T = 0$ at sufficiently low v . In an infinite system, domains continue to increase in size versus time and the system never reaches the true ground state [34] consisting of a single ferromagnetic domain.

The coarsening time scale does not describe the ultimate convergence to the ground state [36]. For m^2 at and above its shoulder feature, we find a different behavior corresponding to a time scale $\propto L^3$, which we demonstrate by graphing the data versus vL^3 in Fig. 3(c).

Here we observe that the shoulder-like feature extends to larger values of the scaling variable as L increases, likely forming a plateau at a constant non-zero m^2 extending to arbitrarily high vL^3 as $L \rightarrow \infty$ (as we will argue in more detail below). Thus, some kind of long-lived defects form in at least a fraction of the SA instances, and it is natural to assume (and we will prove below) that these defects are the system-spanning stripe domains previously found in fixed- T simulations (with an initial stripe state imposed) [63] and instantaneous quenches [59, 60, 62].

We observe the same two time scales also in the excess energy density, which is graphed versus vL^2 and vL^3 in Fig. 4(a) and Fig. 4(b), respectively. In this case, for the data to collapse onto a common scaling function we also have rescaled the observable by the system size L in accord with Eq. (9b). In Fig. 4(a) the small- L corrections to the common curve $f_e(vL^2)$ are even smaller than the more visible corrections to $m^2 \approx 0.6$ in Fig. 3(b). However, clear deviations from scaling collapse are seen for the smaller values of vL^2 on the more detailed scale in the inset of Fig. 4(a). The data in this range again collapse when graphed versus vL^3 , as shown in Fig. 4(b). Here the formation of a plateau with constant excess energy with increasing L is also apparent and corresponds to the less clear build-up toward a constant $m^2 \approx 0.6$ in Fig. 3(c). These plateaus are naturally explainable as consequences of system-spanning defects remaining stable until $T = 0$ without significant change in the mean length of the domain walls, when the confined domains have evaporated away on the faster L^2 time scale. The final low-velocity approach to zero excess energy corresponds to the topological domains finally being broken (after which they can vanish by conventional coarsening), the time of which follows a broad probability distribution at given v , thus giving rise to the smooth evolution from the plateau value of the average energy to zero in Fig. 4(b). The gradually diminishing probability of a stripe domain surviving all the way to $T = 0$ as v is lowered is likewise manifested as m^2 increasing from the plateau value $m^2 \approx 0.6$ and finally approaching 1 in Fig. 3(c).

Assuming that the stripe domains are predominantly of the horizontal or vertical kind, i.e., with winding number $(1, 0)$ or $(0, 1)$, and that only one such defect domain is present, the scaled excess energy density $L(e_z - e_{z,0})$ equals 4 if the domain walls are smooth. The plateau value in Fig. 4(b) tends to a value close to 1.5, which implies that about 40% of the configurations resulting from these SA processes host stripe domains (with the approximation of smooth domain walls). The large number of such samples is consistent with previous studies of sudden quenches [59], where random spin configurations ($T = \infty$) were evolved by MC updates at $T = 0$. In this case, smooth horizontal or vertical domain walls are frozen in and the fraction of such samples, which can be computed exactly [61, 62], is about 0.34. It was also found that diagonal domain walls, such as those illustrated in Fig. 2(c), vanish on a time scale L^a with $a \approx 3.5$ at fixed $T < T_c$ [62], surprisingly being different

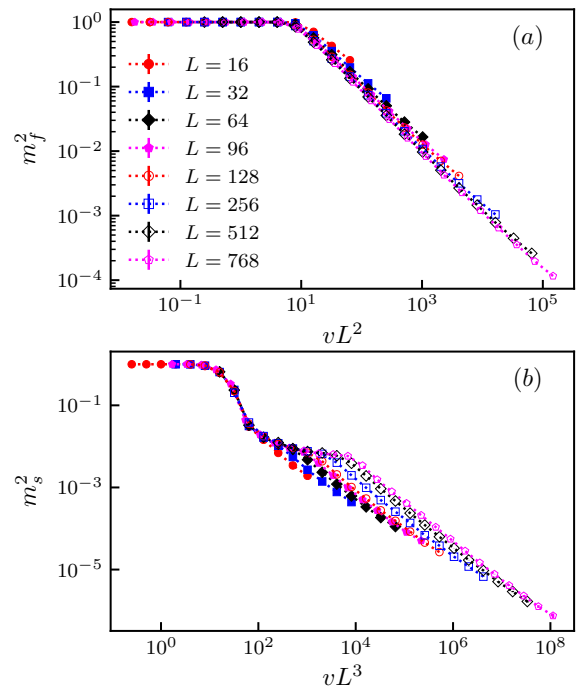


FIG. 5. Data collapse of the grouped squared order parameters; m_f^2 in (a) and m_s^2 in (b), corresponding to averages over the respective 20% of the instances classified as fast or slow according to the value of m^2 . The velocity in (a) and (b) has been rescaled by L^2 and L^3 , respectively, corresponding to the time scale of conventional coarsening dynamics and the slower removal of stripe defects.

from the L^3 scale of elimination horizontal or vertical domains [63] at low $T > 0$. The almost perfect data collapses versus vL^3 in Figs. 3(c) and 4(b) suggests that the value of the exponent is exactly 3. In Sec. II C we will demonstrate explicitly that this L^3 scaling indeed involves only $W = (1, 0)/(0, 1)$ domains.

The L^2 and L^3 scaling behaviors can be further refined by dividing the final spin configurations into two groups according to their m^2 values. A value close to 1 typically means that no large-scale defect is present, and then the L^2 scaling should be more prominent. Conversely, by analyzing the group with small m^2 the L^3 scaling should be better emphasized. Here we define the groups to contain 20% of the total number of configurations; those with the largest and smallest m^2 values, which we refer to as the “fast” and “slow” groups, respectively. As shown in Fig. 5(a), the fast group does not show any deviations from the L^2 time scaling, apart from some scaling corrections for the smaller systems, thus indicating that there are no instances of stripe domains in this group. In Fig. 5(b), there is still L^2 scaling when m^2 is below the value of the plateau that builds up with increasing L , which is natural since the configurations with stripe domains also contain confined domains at high velocity and coarsening is also the mechanism by which a fractal domain in the neighborhood of T_c evolves to a stripe

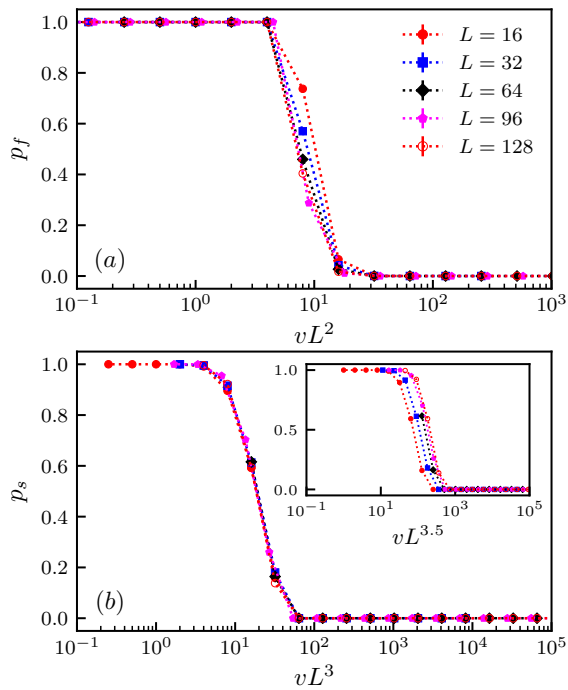


FIG. 6. Probability of reaching one of the perfectly ferromagnetic ground states for the same fast (a) and slow (b) annealing instances as in Fig. 5, graphed against the corresponding scaled velocities vL^2 and vL^3 .

with smoother interfaces in the ordered phase. The ultimate saturation of the order parameter to $m^2 = 1$, which takes place on the time scale L^3 , is still more rapid than in Fig. 3(c) because of less surviving confined domains in the slow group.

Another metric for identifying the relevant time scales is to use the probability of reaching one of the perfect ground states, i.e., the fraction of samples with $m^2 = 1$ after annealing. Fig. 6 shows this probability in the fast and slow groups, again versus vL^2 and vL^3 , correspondingly. The good data collapses further validate the L^2 and L^3 scales. The inset of Fig. 6(b) shows a contrasting plot with the scaling $vL^{3.5}$ expected with the relaxation time observed in sudden quenches [59] (our improved exponent $a \approx 3.42$ for diagonal stripe elimination, determined in Sec. II C, does not alter the plot significantly). In principle, there may be a small correction to the fully saturated magnetization that would be visible in high-precision results for $1 - m^2$. However, we do not have sufficiently many v values and good enough statistics for such an analysis.

It has been argued that the time scale of a straight stripe domain to vanish is $\propto L^3 e^{4J/T}$ in the limit of fixed low temperature [59]: Starting from perfectly straight domain walls, an indentation in one wall, corresponding to a probability $\propto e^{-4J/T}$ of a single-spin flip, provides a seed by which one layer of the defect domain can be peeled off by a random walk without additional energy cost, thus requiring of the order L^2 steps to completely

remove one layer. Removing of the order L layers then leads to the $\propto L^3$ time scale. While this appears a plausible scenario at extremely low temperatures, so that no additional seed defects form within the time $\propto L^3$ taken to eliminate a domain, in reality multiple defects will be present in fluctuating domain walls at higher temperatures. With SA spanning high to low temperatures, the above arguments do not appear to be applicable.

To study the way a stripe domain vanishes, we can identify events during the SA process where the winding number changes from non-zero to zero, which marks the elimination of the last system spanning defect. The topological winding number of a configuration can be computed by assigning positive and negative x or y unit currents to all lattice links associated with domain walls (i.e., those with different spin orientation on either side of the link). Walking along a domain wall from an arbitrary initially selected location, the currents are accumulated until the same location is reached again, repeating such loop-building processes for all domain boundaries in the system. A system without topological defects has no loops with net current, while the current of a topological domain wall is a multiple of the system length L . We normalize such that the winding number is $W = (w_x, w_y)$ with positive components $w_x, w_y \in \{0, 1, 2, \dots\}$. Note that there are restrictions on the winding numbers, e.g., $W = (2, 0)$ is not possible. The probability $P(w_x, w_y)$ decreases rapidly with increasing winding, as will be discussed quantitatively in Sec. II C.

Applying the above method to identify configurations when their winding number change from non-zero to zero (in practice checking the winding after each full MC sweep), we further apply a temperature T^* at which we demand non-zero winding and only output configurations after zero winding is found during the subsequent part of the SA process down to $T = 0$. Fig. 7 shows examples of such recently broken stripe domains generated for a system with $L = 64$ and $T^* = 1.5$. The winding number changed to zero only slightly below T^* in all cases shown. Here it is clear that the still rather thick minority domains have been pinched off by the two interfaces colliding, which is also the mechanism suggested in Ref. [63] at fixed $T < T_c$. While the resulting severed domain may also have been thinning overall before it breaks, there are no long straight segments where the mechanism of diffusion of a single seed defect over large distances can take place. Thus, the $\propto L^3$ time scale that we observe should have a different origin than the low- T mechanism proposed in [60]. A related problem of an interface model driven by deposition and evaporation of particles [64], mapped to a kinetic Ising model, can account for the L^3 scaling, but the exponent is not universal.

We do not observe any signs of a time scale $\propto L^a$ with $a \approx 3.5$ in m^2 or e_z , which suggests that the diagonal stripes in SA vanish faster than those in instantaneous quenches to $T = 0$ [59]. We will show in Sec. II C that the presence of diagonal domains in SA is actually controlled by the KZ mechanism, the time scale $L^{3.17}$ of which is

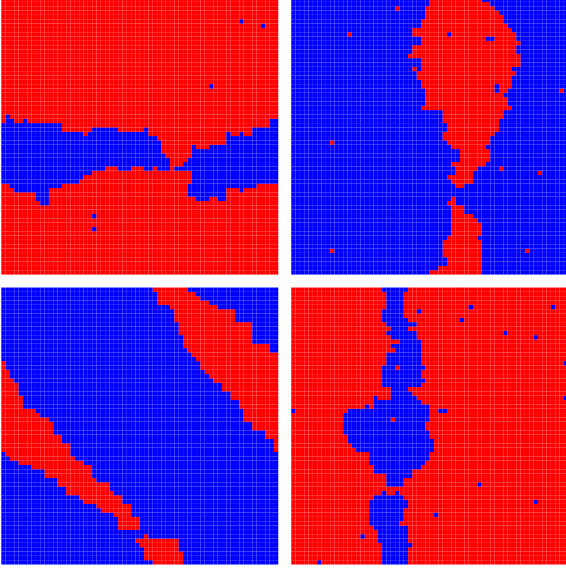


FIG. 7. Snapshots of $L = 64$ spin configurations generated by SA shortly after the winding number changed from non-zero to zero. The minority domains have been cut by the majority species “tunneling” through via interface fluctuations. Events taking place below $T = 1.5$ were singled out.

faster than the corresponding $\propto L^a$ time to eliminate a diagonal domain at fixed $T < T_c$. We will also obtain a more precise estimate of the exponent in fixed- T simulations; $a = 3.42 \pm 0.02$. If the time scale in SA indeed is $L^{3.17}$, we would still expect some impact on m^2 or e_z , specifically a third regime of scaling collapse if the lowest- v data are graphed versus $vL^{3.17}$ instead of vL^3 , i.e., the same data should then be described by three different scaling functions (of vL^2 , vL^3 , and $vL^{3.17}$). However, diagonal domain are relatively rare at $T = 0$ and the presence of scaling corrections and statistical errors make it difficult to separate the two cases with rather similar exponents 3 and 3.17. The winding-number method used in Sec. II C completely isolates the configurations with diagonal domains and enables us to study their decay time more precisely.

To further characterize the path of a system to full ordering via removal of large-scale domains, it is useful to study Fourier modes of the spin texture at small non-zero wave-vector \mathbf{q} ;

$$m_{\mathbf{q}} = \frac{1}{N} \sum_{x,y} \sigma_{xy} e^{-i(xq_x + yq_y)}, \quad (10)$$

where we now have labeled the Ising spins by their lattice coordinates, $x, y \in [0, L - 1]$. The expectation value of $m_{\mathbf{q}}$ vanishes by symmetry but its absolute value squared is useful as a generalization of m^2 . We here take k to mean the longest wavelength along either the x or y axis, $k_x = (2\pi/L, 0)$ and $k_y = (0, 2\pi/L)$, and take the sum of the two squares,

$$m_k^2 = \langle m_{k_x}^* m_{k_x} \rangle + \langle m_{k_y}^* m_{k_y} \rangle, \quad (11)$$

which can indiscriminately detect system-spanning domains forming parallel to either the x or the y axis. For such a stripe of relative width x/L (which we here treat as a continuous variable even for finite L) and completely smooth domain walls, the uniform magnetization is

$$m = \pm \left(1 - \frac{2x}{L}\right), \quad (12)$$

while the squared long-wavelength order parameter is

$$m_k^2 = \frac{2[1 - \cos(\frac{2\pi x}{L})]}{\sin^2(\frac{\pi}{L})L^2}. \quad (13)$$

By expressing x/L as a function of m^2 and then rewriting m_k^2 in terms of m^2 , we obtain the following form of m_k^2 as a function of m^2 :

$$m_k^2 = \frac{2[1 - \cos(\pi(\sqrt{m^2} + 1))]}{\sin^2(\frac{\pi}{L})L^2}. \quad (14)$$

While typical domain walls are not smooth, the limiting case is still useful. We have also calculated similar functional relationships between m^2 and m_k^2 for spin configurations with a single perfectly square or circular defect.

Figure 8 shows scatter plots of m_k^2 versus m^2 for $L = 64$ systems annealed over 2^n MC steps with three different values of n . The functional forms of m_k^2 versus m^2 for the straight system-spanning domains as well as the circular and square-shaped confined domains are also shown. For long SA processes, most instances land on the point $(m^2, m_k^2) = (1, 0)$ representing the two uniform ferromagnetic ground states. As expected, Eq. (14) for smooth domains represents the upper bound for m_k^2 given m^2 . The instances containing straight domain walls concentrate closer to this bound as the annealing time is increased, especially in Fig. 8(c), showing that the remaining domain walls become smoother as the annealing time is increased. In Figs. 8(a) and (b), many points also are accumulated close to the curves representing square and circular domains, with the former providing an upper bound for all confined domains. However, in Fig. 8(c) there are no configurations left in the region of confined domains, while many instances of straight domains remain, reflecting the longer time required for eliminating the latter in the instances where they are present. There are also points near the low-left corner of the diagrams, which correspond mainly to configurations with diagonal stripe domains, for which both m^2 and m_k^2 vanish in the ideal case of smooth domain boundaries. These domains could also in principle be analyzed as above by using the appropriate wave-number \mathbf{q} in Eq. (10). Instead, in Sec. II C we will analyze the probability distribution of the topological winding number.

B. System-spanning domains at fixed T

Before further studies of the SA life time of system-spanning domains, we return to the question of these

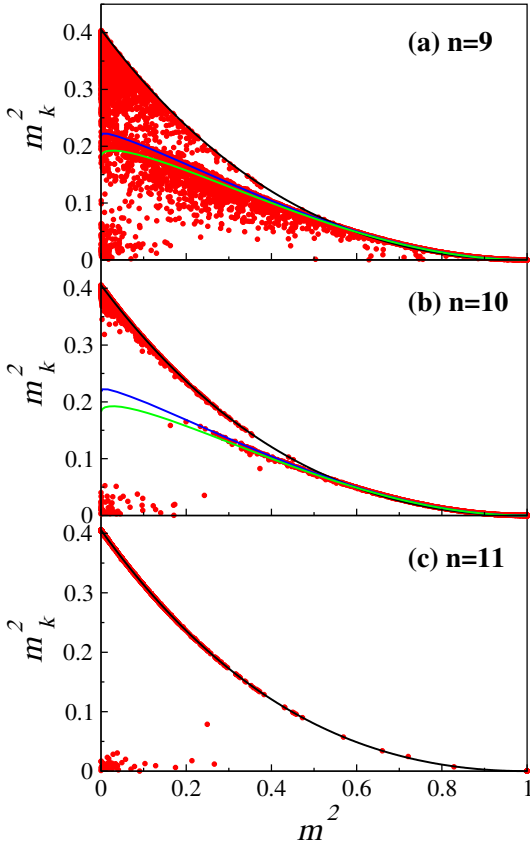


FIG. 8. Scatter plots of the domain order parameter m_k^2 , Eq. (11), vs the conventional order parameter m^2 for thousands of instances of an $L = 64$ system annealed from $T = 4$ to $T = 0$ in 2^n steps with $n = 9$ in (a), $n = 10$ in (b), and $n = 11$ in (c). The black curves show the function Eq. (14) for systems with perfectly straight stripe domains, while the blue and green curves in (a) and (b) indicate, respectively, such relationships for systems with single circular and square shaped domains. In (c), most of the instances ended at $m^2 = 1$, $m_k^2 = 0$. The points with small m^2 and m_k^2 , in the low-left corners, correspond predominantly to systems with a remaining diagonal stripe defect.

time scales at fixed $T < T_c$. To this end, we initialize the system in a state of two domains, with $3/4$ the spins up and $1/4$ down and smooth domain walls, either horizontal (the case first studied in Ref. [63]) or diagonal (studied at $T = 0$ in Ref. [59]). These spin configurations have winding number $W = (1, 0)$ and $(1, 1)$, respectively. Our aim is to confirm that these domains are really eliminated on different time scales, by studying larger systems than previously. We perform MC simulations at fixed temperature significantly below T_c and compute the the winding number after each MC sweep. If $W = (0, 0)$, which indicates that there is no longer a system-spanning defect domain in the system, the simulation stops and the number τ_d of MC sweeps performed is recorded. This procedure is repeated many times for a mean decay time $\langle \tau_d \rangle$. In addition, the logarithm of τ_d is also averaged for

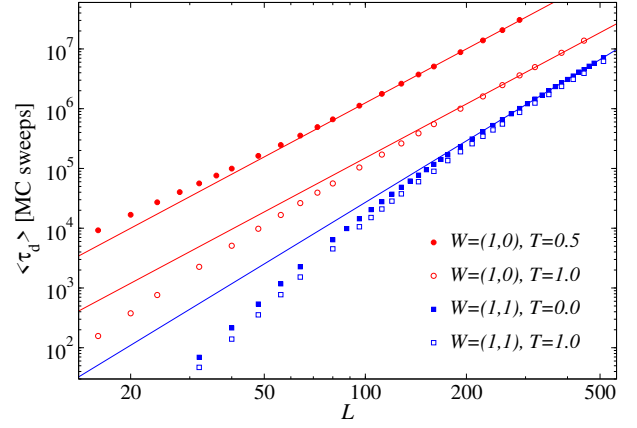


FIG. 9. Mean time required at fixed $T < T_c$ to remove a system-spanning minority domain (consisting of $1/4$ of the spins) imposed in the starting configuration. Size dependent results are shown at two different temperatures each for horizontal, $W = (1, 0)$, and diagonal, $W = (1, 1)$, domains. The red lines drawn through the $W = (1, 0)$ large-size data correspond to L^a power laws with $a = 3$. The blue line is a fit to the $W = (1, 1)$ data at $T = 0$ for $L \geq 288$, with the resulting exponent $a \approx 3.42$. All error bars are much smaller than the plot symbols.

an estimate $\exp(\ln(\tau_d))$ of the typical time.

The mean decay time is graphed versus the system size in Fig. 9 for both types of domains at two different temperatures. In the case of $W = (1, 0)$ the expected form $\langle \tau_d \rangle \propto L^a$ with $a = 3$ is fully consistent with the large- L data. A fit to the better size-converged $T = 0.5$ data set gives $a = 2.987 \pm 0.013$ (the error indicating one standard deviation of the mean) when using data for $L \geq 128$ (for a statistically good fit). Fitting to the typical decay time (data not shown here) for the same range of system sizes gives a statistically equal exponent, $a = 3.008 \pm 0.014$, thus showing that the distribution of decay times does not have broad tails. The results for $T = 1$ are also fully consistent with $a = 3$ but, because of the slower convergence to the asymptotic form, the statistical errors are larger.

Note that the prefactor of the L^3 form (the constant shift on the log scale used in Fig. 9) for $W = (1, 0)$ is much larger at the lower temperature, which reflects the reduced domain-wall fluctuations with lowered T , with eventual freezing of domains with smooth walls at $T = 0$. For $W = (1, 1)$, only a very weak dependence on the temperature is seen Fig. 9, which is clearly related to the fact that the diagonal domains can decay away also at $T = 0$ (the lower temperature in Fig. 9) and, apparently, non-zero temperature does not significantly assist in the large-scale interface fluctuations in this case. Fits to the $T = 0$ data for $L \geq 288$ gives the exponent $a = 3.420 \pm 0.015$ for the mean decay time and 3.556 ± 0.016 for the typical time (for which data are not shown). The exponent for the mean time is roughly consistent with the less precise result $a \approx 3.5$ in Ref. [59], where the system sizes were

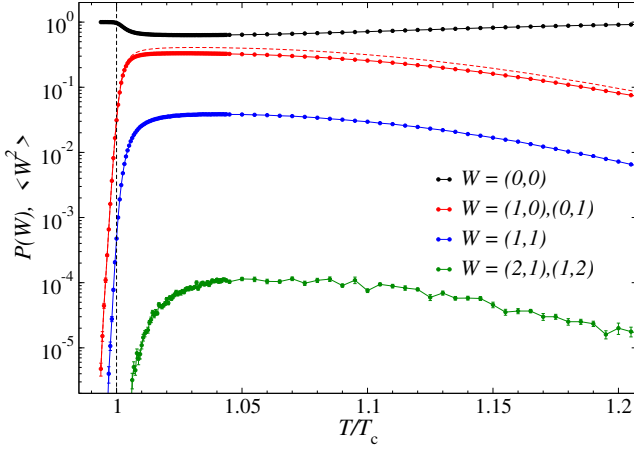


FIG. 10. Temperature dependent probabilities of the four dominant winding number sectors obtained by equilibrium SW simulations for lattice size $L = 512$. The $w_x \neq w_y$ results represent the sum of the two equivalent probabilities. The red dashed curve is the mean squared winding number.

smaller and the typical decay time was not addressed. We also tested whether the data could potentially instead be described by L^3 with a multiplicative logarithm (also including an exponent on the log). However, the parameters of this fit do not stabilize when the smaller sizes are gradually excluded. The $T = 1$ results are also consistent with a pure L^a form, with the same exponents as the $T = 0$ case; $a = 3.432 \pm 0.024$ for the mean decay time and $a = 3.564 \pm 0.024$ for the typical time, again from fits to the $L \geq 288$ data. Thus, for the diagonal domains it appears that the mean and typical time scales are different. Both the mean and typical exponents for diagonal walls are larger than the KZ exponent $z + 1/\nu \approx 3.17$, which is very significant in the context of SA, as will be discussed next.

C. Winding number analysis

The fact that the time scale L^3 for elimination of straight domain walls below T_c is shorter than the KZ scale $L^{3.17}$ implies that their survival probability in the ordered phase is not governed by KZ scaling. Conversely, KZ scaling can be expected to apply to the persistence of diagonal domain walls, since their time scale for elimination at $T < T_c$ is longer, of order $L^{3.42}$. This is a very interesting prospect in the context of the original KZ ideas [26, 27], which concerned large-scale topological defects akin to the system-spanning domain walls in the Ising model. In addition to confirming KZ scaling for the $W = (1,1)$ diagonal domains in $T \rightarrow 0$ SA, we will here also show additional evidence for the faster scaling of the $W = (1,0)/(0,1)$ horizontal/vertical domains. We do this by explicitly studying probabilities of different winding numbers, first in equilibrium MC simulations and then with SA. Strictly speaking, the prob-

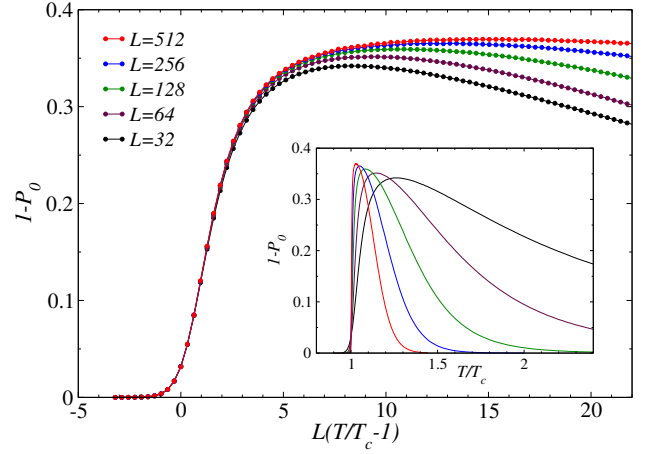


FIG. 11. Critical scaling with the 2D Ising exponent $\nu = 1$ of the probability of non-zero winding number in equilibrium SW simulations. The inset shows the raw data before scaling, with the same color coding as in the main graph. Error bars are too small to be visible.

abilities presented below were computed on the basis of the largest winding number of an individual domain wall found in the generated spin configurations, i.e., $P(W)$ is the probability of $W = (w_x^2 + w_y^2)^{1/2}$ being the largest winding number among any of the domain walls in a sampled configuration. The probability of more than one winding domain in the same configuration is very low, a manifestation of which is that the probabilities in the four winding sectors reported below almost completely exhaust the mean of the squared winding number computed with all domain walls.

For the equilibrium simulations the Swendsen-Wang (SW) cluster algorithm [73] was used for system sizes up to $L = 512$. The temperature dependence of the probabilities of the sampled configurations to fall in one of the four most important winding number sectors is shown in Fig. 10 for the largest system studied, along with the mean squared winding number. All $W \neq (0,0)$ probabilities vanish for $T \rightarrow \infty, L \rightarrow \infty$ because of the zero percolation probability in the paramagnetic phase. The winding probabilities also have to vanish for any T below T_c in the thermodynamic limit because of the large $\propto L$ internal-energy cost of system-spanning domain walls. There is significant size dependence overall, but the peak values in Fig. 10 are close to converged, and also close to the exact probabilities [62] (slightly larger for non-zero winding) in quenches of random states to $T = 0$ (and there is no reason for these probabilities to be exactly the same). The non-zero W probabilities indeed drop very rapidly in the neighborhood of T_c .

All the distributions $P(W)$ exhibit critical scaling in the form expected for a dimensionless quantity. Fig. 11 shows $1 - P(0,0)$, i.e., the probability of a spin configuration having at least one winding domain, versus the distance $\delta = T/T_c - 1$ to the critical point scaled by $L^{1/\nu} = L$. The data collapse well onto a common scal-

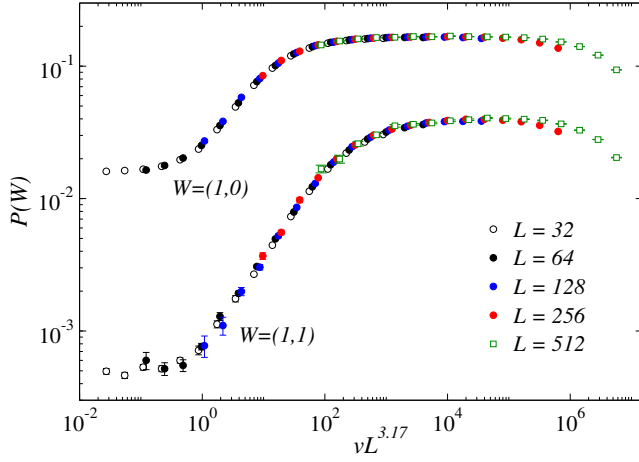


FIG. 12. Scaling of the probability of winding numbers (1,0) and (1,1) in SA runs ending at T_c for five different system sizes. The velocity has been scaled with the system size according to the expected KZ exponent $z + 1/\nu \approx 3.17$.

ing function $p(\delta L)$ close to T_c , and a constant behavior emerges for large δL with increasing system size. The suppression of winding in the neighborhood of T_c is again very prominent. We note that the extended domain walls existing in the 2D Ising model at T_c are fractal and can be described by conformal field theory [74, 75].

Next, we turn to the out-of-equilibrium simulations, again performed with standard Glauber dynamics. In this case the SA starting temperature was $2T_c$. KZ scaling of the winding probabilities at T_c is confirmed in Fig. 12 with the examples of $W = (1,0)$ and $(1,1)$. Here $P(1,0)$ refers to only $W = (1,0)$, though the equivalent $(0,1)$ probability was used for averaging. Note that the maximum values of the velocity-scaled probabilities in Fig. 12 are very close to the peak values slightly above T_c in the corresponding equilibrium results for $L = 512$ in Fig. 10 [adjusted by the factor 2 in the case of $W = (1,0)$]. This behavior reflects the similarity of the near-critical state at mildly elevated $T > T_c$ ($T - T_c \sim L^{-1/\nu}$) in equilibrium and the slightly out-of-equilibrium state in SA when stopping at T_c —both temperature and velocity effects enhance the presence of system-spanning winding domains.

For SA continuing all the way to $T = 0$, Fig. 13(a) reveals the L^3 scaling of the $W = (1,0)$ probability, as should be expected based on the results in Sec. II A. However, the $W = (1,1)$ data do not collapse well versus vL^3 . Instead, scaling the velocity with the KZ time $L^{z+1/\nu}$ produces excellent data collapse, as shown in Fig. 13(b). This difference between the two winding sectors is consistent with the time scale $L^{3.42}$ found in Sec. II C for the elimination of the diagonal domain walls at fixed $T < T_c$. The KZ scale is shorter and, therefore, the $W = (1,1)$ domains will primarily decay very soon after T_c has been crossed (and even slightly before, judging from the peak locations in Fig. 10), with a slower decay rate during the part of the SA process from T_c down to

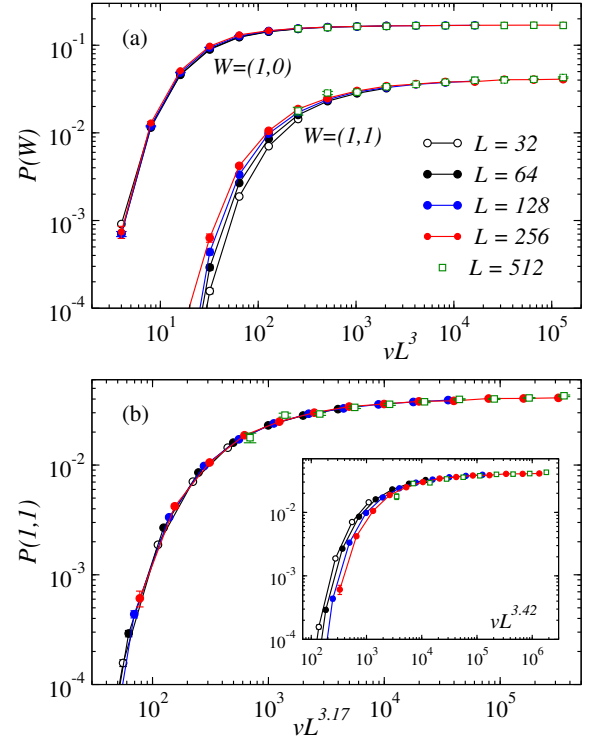


FIG. 13. Scaling with v and L of the probability of winding numbers (1,0) and (1,1) after SA to $T = 0$. In (a), both data sets are graphed vs vL^3 , which leads to good data collapse for the five system sizes considered only for $W = (1,0)$. Note that many of the $L = 512$ data points over those for the smaller systems. In (b) the $W = (1,1)$ data are instead collapsed vs $vL^{3.17}$, corresponding to KZ scaling. The inset of (b) demonstrates the absence of data collapse when v is scaled by $L^{3.42}$; the fixed- T scale of diagonal domain elimination.

$T = 0$ so that KZ scaling remains valid even at $T = 0$. Scaling with $L^{3.42}$ does not produce good data collapse (except in the almost flat portion that is not sensitive to small variations in the exponent), as shown in the inset of Fig. 13(b).

The fast decay of the winding probabilities immediately below T_c is confirmed in Fig. 14, which shows $L = 256$ results accumulated after each segment of $1/64$ of the total number of annealing steps. After the initial drop, the probabilities only decay slowly as T is further lowered. The slow evolution in the case of $W = (1,1)$ is perhaps surprising in light of the mean times to eliminate diagonal stripe domains at fixed T in Fig. 9, which for $L = 256$ is not much longer than the almost flat portion during the SA process at $v = 2^{-12}$ in Fig. 14(b). However, it should be kept in mind that the fixed- T runs were started with rather thin domains (containing $1/4$ of the spins), while the domains remaining after the initial steep decay in SA are those that are the most difficult to eliminate. In the case of $P(1,0)$, the tendency to further decay at low temperatures is more obvious, especially in the case of the lowest v in Fig. 14(a). Because of the overall much smaller scale of the $P(1,1)$ probabilities,

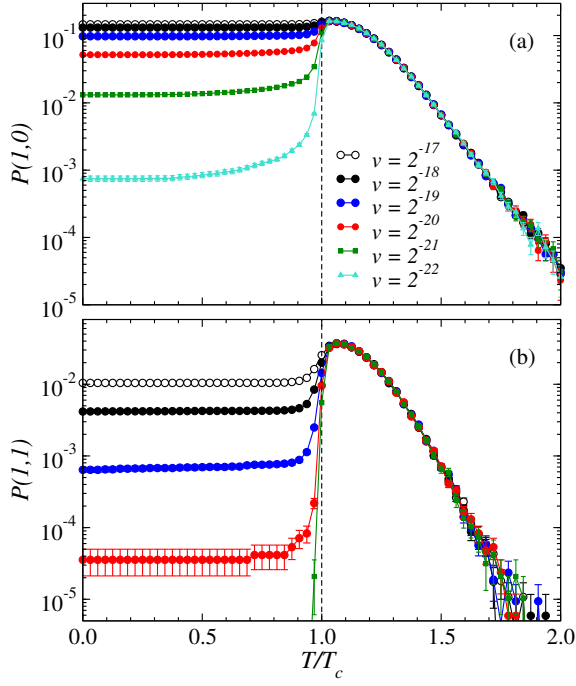


FIG. 14. Temperature dependent probability of winding number (1,0) (a) and (1,1) (b) during SA from $T = 2T_c$ to $T = 0$. The results are for fixed system size $L = 256$ and different velocities v , with v^{-1} being the total annealing time.

statistically meaningful $T \rightarrow 0$ results were limited to higher velocities in Fig. 14(b).

D. Open boundary conditions

The characterization of a system-spanning domain wall by a specific winding number is not possible in an open system. Moreover, in this case there is only a single domain wall in a configuration with two domains. Nevertheless, the ends of such domain walls touch opposite edges of the system and that also prohibits shrinkage of a domain in the “long” direction until an interior point of the domain wall reaches an edge, thus breaking one of the domains up into two pieces. Alternatively, the end points of the domain wall can simply migrate toward each other on adjacent edges and shrink one of the domains that way. It is not a priori clear whether the fluctuations of these long domain walls should be qualitatively different from those in a periodic system, and what the time scale of elimination of system-spanning domains are.

Open boundary conditions are of interest in the context of QA experiments because periodic boundaries cannot be easily accessed with some of the current platforms, such as Rydberg atom arrays [24, 25]. With superconducting qubit arrays periodic boundary conditions can be implemented by constructing logical qubits consisting of two physical qubits, as has been done with D-Wave devices [17]. A larger number of couplers in the most re-

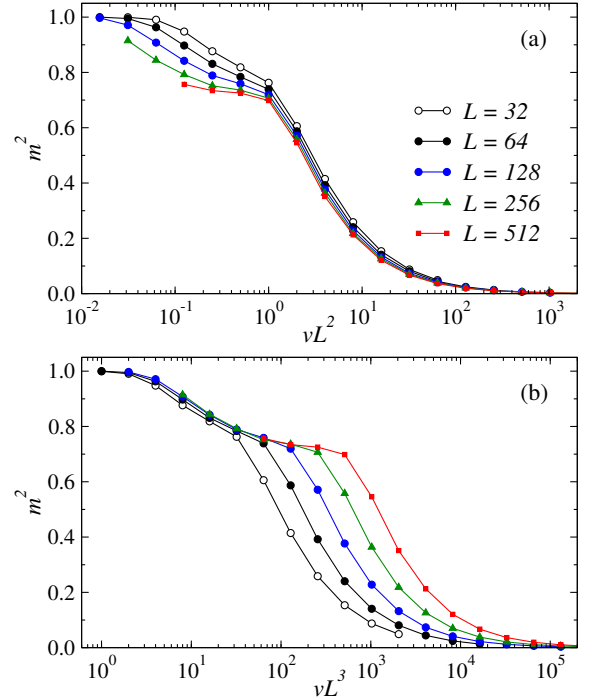


FIG. 15. Squared order parameter of systems with open boundary conditions at the end of $T \rightarrow 0$ SA runs for different velocities and system sizes. The data are analyzed in the same way as those for the periodic systems in Figs. 3(b) and 3(c), revealing the times scales L^2 in (a) and L^3 in (b). Error bars are at most of the size of the plot symbols (for $L = 512$ at the lowest- v points).

cent D-Wave device allows for fully periodic boundaries of 2D square lattices with up to 12×12 native qubits [19] (larger cylindrical lattices, i.e., periodic in only one direction, have been also implemented [18]). It will still be useful to also investigate open boundaries. In SA, we here focus on system-spanning domain walls and their time scales, and we expect the results to also be relevant in the context of QA (for which we will only consider small periodic lattices in Sec. III).

We first confirm the presence of both the L^2 and L^3 time scales also in open systems by studying m^2 after SA to $T = 0$, starting at $T_{\text{ini}} = 2T_c$. Fig. 15 shows scaled results analogous to those for periodic systems in Figs. 3(b) and 3(c). The data for open systems collapse in the same way, with only slightly larger corrections, and overall the shapes of the collapsed data (the scaling functions) look very similar. The L^3 scale is again presumably related to horizontal or vertical domain walls.

To specifically investigate the fate of diagonal domain walls in open systems, we carry out calculations at fixed $T < T_c$ with a domain wall imposed initially, in analogy with Sec. IIB for the periodic systems. Since a diagonal domain wall can be eliminated by local MC updates also at $T = 0$ (and, moreover, Fig. 9 shows only weak T dependence for diagonal domains in periodic systems), we focus on that limiting case. A diagonal domain wall is

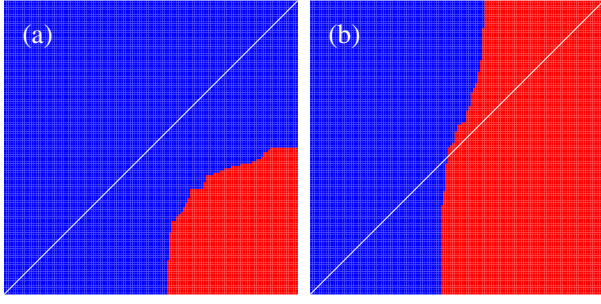


FIG. 16. Configurations from MC simulations of a system of size $L = 128$ at $T = 0$, obtained by starting from a configuration in which the spins below and above the $x = y$ diagonal (the white lines) are all up (red) and all down (blue), respectively. The spins exactly on the diagonal were initially generated at random. The fluctuations of the domain wall over time eventually leads to either (i) a fully ferromagnetic state, the fate of the case in (a), or (ii) a state with two domains separated by a stable (at $T = 0$) horizontal or vertical smooth domain wall to which the (b) configuration will evolve.

created by randomly generating up and down spins on the $x = y$ line on open $L \times L$ lattices and setting all the spins below (above) this line to up (down). A spin can only be flipped if the energy is lowered or stays the same, and we carry out N such attempts at random locations for each time unit. This $T = 0$ MC simulation could in principle be made much more efficient by only considering spins adjacent to the single fluctuating domain wall, which we did not implement because very large systems are not needed for our conclusions here.

The single domain wall, with end points that are initially on opposite corners of the square lattice, can evolve in two qualitatively different ways that are illustrated with representative spin configurations in Fig 16: (i) The end points move to adjacent edges and continue to gradually move toward each other while the length of the wall is reduced over time, thus creating a shrinking domain in one corner of the system and eventually leading to the fully ferromagnetic state. Such a case of a shrinking corner domain is shown in Fig 16(a). (ii) The end points move to opposite edges of the lattice and the domain wall becomes increasingly horizontal or vertical with time, which also shortens it and reduces its energy from that of the initially diagonal wall. Eventually a completely straight wall is formed that cannot evolve further. A configuration where such a stable domain wall ultimately forms is shown in Fig. 16(b). Whichever of the cases (i) and (ii) is realized depends on the very early stages of the MC process. We have confirmed to high statistical precision that the probability is 1/2 for both, as would be expected based on the equal probabilities of initial fluctuations of the end points of the wall to either adjacent or opposite edges of the lattice.

Despite the system-spanning initial domain wall, the mean time to evolve to the fully ferromagnetic state in case (i) scales as L^2 , i.e., the conventional coarsening

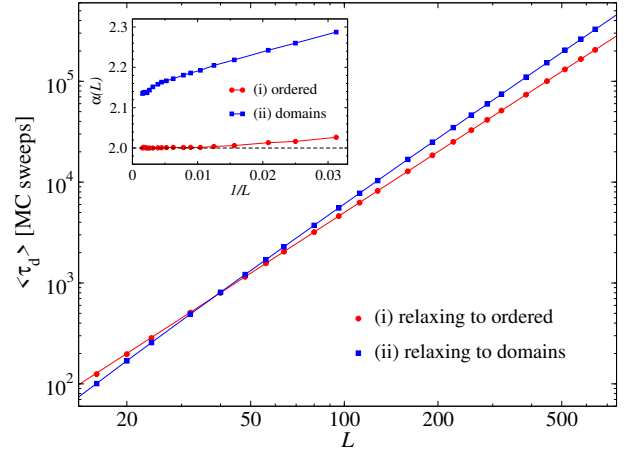


FIG. 17. Size dependence of the mean time at $T = 0$ for systems with an initially imposed diagonal domain wall to evolve into (i) a fully ferromagnetic state (red circles) or a (ii) stable state with a straight domain wall (blue squares), as illustrated in Fig. 16. The red fitted line has the form $\langle \tau_d \rangle \propto L^2$, while the blue curve is from a fit including also a multiplicative log correction; $\langle \tau_d \rangle \propto L^2 \ln^a(L/b)$, with $a = 0.72$ and $b = 1.7$. Error bars are much smaller than the plot symbols. The inset shows size dependent exponents $\alpha(L)$ obtained from data for pairs of system sizes $(L, 2L)$ under the assumption of pure power laws $\propto L^\alpha$. The results for case (ii) are consistent with a log correction to the exponent $\alpha(L)$ while in case (i) the corrections are small and conventional.

time, as shown with the red symbols and a fit in Fig. 17. However, in case (ii) the time to reach a stable straight domain wall is slightly longer and can empirically be described by L^2 with a multiplicative log correction, as shown with the blue symbols and the fitted function in Fig. 17. A plain log correction works for all but the smallest few system sizes, but with an exponent ≈ 0.7 on the logarithm also the smallest systems can be accounted for. The inset of Fig. 17 shows running exponents for both cases (i) and (ii) obtained from data for system sizes L and $2L$ by assuming the form $\langle \tau_d \rangle \propto L^\alpha$. Here a rapid convergence to $\alpha = 2$ is seen for (i), while for (ii) the values decrease slowly with increasing L in a way consistent with a log correction. Thus, we conclude that, even in the setting of open boundaries, the anomalous fluctuations of the diagonal domain wall survive, now leading to a correction to conventional coarsening, even though in this case the state can only be classified as having a diagonal domain wall at the initial stages of the simulation. We note again that the time scaling of diagonal stripe domains in periodic systems, Fig. 9, is not well described by L^3 with a log correction but really seems to demand a different power law; $\langle \tau_d \rangle \propto L^{3.42}$.

While the resulting straight domain wall in case (ii) is stable at $T = 0$, at $T > 0$ the interface can again fluctuate, and once a point reaches an edge of the system one of the domains is severed and can decay away by coarsening as in case (i). The time scale of the domain wall colliding with an edge should be the same as that of two walls

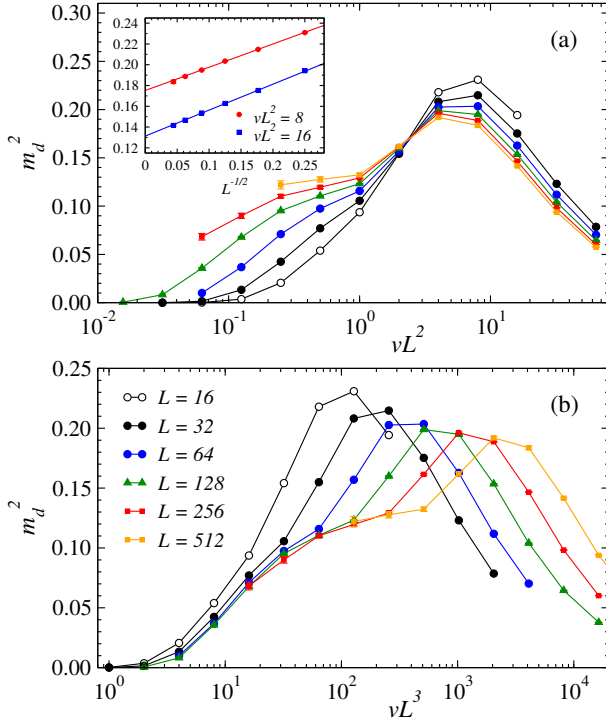


FIG. 18. The domain-wall order parameter defined in Eq. (16) computed in SA for different system sizes and velocities. The size legends in (b) also apply to (a). The data are graphed with the velocity rescaled by the conventional coarsening time scale L^2 in (a) and by the scale L^3 corresponding to domain-wall elimination interface fluctuations in (b). In the inset, the data for $x = vL^2 = 8$ and 16 are graphed versus the square-root of the inverse system sizes along with fits to the form $a + bL^{-1/2}$ with free parameters a and b .

colliding in the periodic systems, thus explaining the L^3 scaling in Fig. 15(b). We can also explicitly confirm the origin of the L^3 scale in SA of open systems by defining a domain-wall order parameter similar to m_k^2 in Eq. (11). Here we simply transform the spins by functions $r_x(x, y)$ and $r_y(x, y)$ of unit magnitude that change signs when crossing the vertical and horizontal central axis of the lattice, respectively, i.e., with $x, y \in \{0, \dots, L-1\}$ we have $r_x(x < L/2, y) = 1$ and $r_x(x \geq L/2, y) = -1$ and similarly for y in $r_y(x, y)$. The order parameter detecting a vertical domain wall is then defined as

$$m_{dx} = \frac{1}{N} \sum_{x,y} r_x(x, y) \sigma_{x,y}, \quad (15)$$

along with an analogous definition of m_{dy} to detect a horizontal domain wall. We compute the corresponding mean squared order parameter

$$m_d^2 = \langle m_{dx}^2 \rangle + \langle m_{dy}^2 \rangle. \quad (16)$$

Figs. 18(a) and 18(b) show results versus the velocity scaled by L^2 and L^3 , respectively, averaged over the final $T = 0$ configurations after SA starting at $T = 4$. Data collapse when plotting versus $x = vL^2$ is not completely

apparent in Fig. 18(a), though the peak value seems to converge with increasing L and the data on the right-hand size of the peak also seem to approach a common scaling function. Convergence is demonstrated in the inset of Fig. 18(a) with data at $x = 8$ and $x = 16$, where fits with square-root corrections to non-zero $L \rightarrow \infty$ values match the data very well. The domains at T_c are fractal in equilibrium and at low velocity, and data collapse when using the time scale L^2 should correspond to coarsening dynamics initially bringing some of the SA instances toward a state with a non-fractal domain wall (and the instances with only confined defects will have very small values of m_d^2 , vanishing for $L \rightarrow \infty$). The data for lower vL^2 do not collapse but do so when instead graphing versus vL^3 in Fig. 18(b), which shows a size independent plateau building up with increasing system size. This plateau reflects the stabilization on the longer survival time scale L^3 of a system-spanning domain wall (in some of the SA instances, as in the periodic systems in Sec. II A). Here the plateau value not only reflects the fraction of instances with a domain wall, but also an average over all the possible locations of the domain wall that determine the value of m_{dx} , Eq. (15), or the similarly defined m_{dy} . In principle some refined domain-wall order parameter could be defined to maximize the signal, e.g., associating values 1 and 0 with the presence and absence, respectively, of a system-spanning domain wall identified using a simple modification of the winding number calculation in Sec. II C. However, the current definition m_d^2 is convincing enough for drawing our conclusions on the L^3 time scale of domain walls here.

III. QUANTUM ANNEALING

For the purpose of QA, we here write the Hamiltonian Eq. (1) with time dependent couplings as

$$H(t) = -J(t) \sum_{\langle ij \rangle} \sigma_i^z \sigma_j^z - \Gamma(t) \sum_i \sigma_i^x, \quad (17)$$

with the following time dependence:

$$J(t) = \left(\frac{t}{t_{\max}} \right)^2, \quad \Gamma(t) = \left(1 - \frac{t}{t_{\max}} \right)^2. \quad (18)$$

The quadratic form at $t = 0$ is chosen to reduce non-analyticity at the beginning of the protocol. The forms of $J(t)$ and $\Gamma(t)$ are also reminiscent of those in D-Wave devices [11, 12, 15, 17], which along with Rydberg atom arrays [21–25] likely present the best experimental platform to which our results can be applied.

The process starts at $t = 0$ with the system prepared in the ground state of the transverse field, followed by evolution under the time dependent Schrödinger equation to $t = t_{\text{QA}}$. For conventional physical observables, we calculate the squared magnetization, the total energy density, and the Ising energy [without the factor $J(t)$]

density:

$$m^2 = \left\langle \psi(t) \left| \left(\frac{1}{N} \sum_{i \in N} \sigma_i^z \right)^2 \right| \psi(t) \right\rangle, \quad (19a)$$

$$e = \left\langle \psi(t) \left| \frac{H(t)}{N} \right| \psi(t) \right\rangle, \quad (19b)$$

$$e_z = \left\langle \psi(t) \left| \frac{1}{N} \sum_{\langle ij \rangle} \sigma_i^z \sigma_j^z \right| \psi(t) \right\rangle. \quad (19c)$$

We also compute the fidelity, i.e., the probability of the system in the evolved state $|\Psi(t)\rangle$ to be in the instantaneous ground state $|\Psi_0(t)\rangle$ of H ;

$$F_{\text{GS}}(t) = |\langle \Psi_0(t) | \Psi(t) \rangle|^2. \quad (20)$$

In practice it is convenient to analyze the (natural) logarithm with a minus sign, $-\log F_{\text{GS}}$, which is positive and approaches 0 as $v \rightarrow 0$. We refer to it as the log fidelity.

We study these quantities as functions of the ratio $s(t) \in [0, 1]$ between the instantaneous time t and the total time for annealing to the classical limit,

$$s = t/t_{\text{max}}, \quad (21)$$

focusing on the observables at the classical limit $s = 1$ of the process and at the point $s = s_c$ where the system is critical in the adiabatic limit,

$$s_c = \frac{1}{1 + \sqrt{(\Gamma/J)_c}} \approx 0.3643, \quad (22)$$

where we use $(\Gamma/J)_c = 3.04458$ [52]. Because of the small system sizes, the results are insensitive to small deviations from the true critical point. For scaling analysis, we consider a wide range of annealing velocities, $v = 1/t_{\text{QA}}$, and system sizes $L \in \{3, 4, 5, 6\}$.

Unlike the classical Ising model discussed in Sec. II, time evolution the 2D TFIM is a computationally challenging problem and there are few reliable numerical results. While the corresponding 1D system can be mapped to free fermions and has been studied exactly on large length and time scales [15, 28–33, 71, 72], the 2D model can be studied in real time only with methods limited to small lattices and/or short times. Beyond exact calculations for small systems that we report on here (and for which we are not aware of previous comprehensive work), recent research on the TFIM and other quantum many-body systems have focused on efficient methods based on the time dependent variational principle in the context of matrix- and tensor-product states [46, 76–82], neural-networks [83], and other variational wave functions [47, 84–86]. While the above methods represent impressive developments, there are still severe limitations in reaching long times with maintained fidelity [18, 45].

Instead of resorting to more advanced but approximate methods, we here carry out exact time evolution for small

lattices but with essentially no restrictions on the annealing time. For the integration of the Schrödinger equation we work with an exact representation of the wave function, taking advantage of all lattice symmetries (translational and point-group) and the \mathbb{Z}_2 spin-reflection symmetry. Thus, we work in the restricted Hilbert space in the same fully symmetric sector as the initial state with $\sigma^x = 1 \forall i$, i.e., zero momentum and even wave function with respect to all reflections and rotations. The number of states in this symmetry block is about 2×10^8 , and extending the calculations to $L = 7$ would not be feasible. We solve the Schrödinger equation using an explicit Runge-Kutta method of order 8(5,3) with adaptive step size [87]. The absolute and relative tolerances for the step size adjustment were set to 10^{-12} .

A. Kibble-Zurek Scaling

KZ scaling in the TFIM has in the past been accessed using quantum MC methods implementing imaginary-time evolution, for which the exponents are the same as in real time though the scaling functions are different [49–52]. Critical scaling has also been recently studied by simulations mixing classical and quantum fluctuations [88]. For the purpose of comparing with QA experiments, true real-time results are required, however. We here test for real-time KZ scaling in the $L \leq 6$ systems at the infinite-size quantum-critical point s_c and, in the case of the fidelity, also at the final point $s = 1$. Other quantities do not exhibit KZ scaling at $s = 1$ and we study their different scaling properties in that limit in Sec. IIIB.

To use the KZ finite- L ansatz Eq. (4) for QA ending at the critical point, we need the critical exponents for the different quantities discussed above. The generic finite-size scaling exponent κ/ν can also be expressed with the scaling dimension Δ_A of the observable A ; $\kappa/\nu = \Delta_A$. The quantum-critical point of the 2D TFIM is in the universality class of the 3D classical Ising model ($d + z$ dimensions with $d = 2$ and $z = 1$), following from the mapping to $2 + 1$ space-time dimensions. Very precise values for the scaling dimensions are available [89]. In the case of the full energy density e , the scaling dimension is that of the Hamiltonian itself; $\Delta_e = d + z$. The Ising interaction and the transverse field can both drive the transition without changing the symmetry [and in our QA protocol Eq. (18) they change simultaneously]; thus they have the same scaling dimensions $\Delta_{e_z} = \Delta_{e_x}$, and this value also defines the correlation-length exponent ν ; $1/\nu = d + z - \Delta_{e_z}$, with $\Delta_{e_z} = 1.412625$ and, therefore, $1/\nu = 1.587375$. For the squared order parameter $\Delta_{m^2} = 2\Delta_m = 2\beta/\nu = 1.036298$, where β is the standard exponent of the order parameter.

As a first test of KZ scaling it is useful to consider the fidelity, Eq. (20), the logarithm of which approaches zero in the adiabatic limit. The time evolution of the log fidelity is shown in Fig. 19 for all the systems that we have studied. Here the total annealing time is scaled

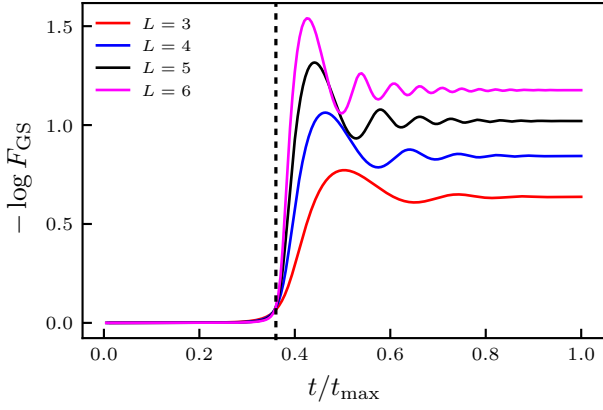


FIG. 19. Log fidelity vs time during QA for different system sizes. The total annealing time is increased with the system size as $t_{\max} = L^2$. The dashed line indicates the known equilibrium critical point for $L \rightarrow \infty$.

with the system size as $t_{\max} = L^2$ as an example. We have also marked the location of the critical point. The fidelity indeed starts to decrease sharply as this point is traversed, with the graphed $-\log F_{\text{GS}}$ exhibiting a steep increase followed by a peak of height that increases with L . This behavior implies that the QA time t_{\max} must increase faster than L^2 in order to keep the system near adiabatic (F_{GS} close to 1), which, as we will see below, is in accord with KZ scaling. We will here not be concerned with the oscillations in $-\log F_{\text{GS}}$ that take place inside the ordered phase in Fig. 19, but note the flattening out to almost constant as the classical limit is approached for all the system sizes. This behavior reflects the growing gap between the ground state and the excitations for $\Gamma > \Gamma_c$ (the gap minimum being at Γ_c with small finite-size corrections), which allows the excited states to thermalize among themselves at the instantaneous value of $s(t)$ [86, 90, 91] while the probability of the system being in the instantaneous ground state is conserved.

The fidelity is a dimensionless quantity in scaling and we can then test the corresponding KZ ansatz,

$$-\log F_{\text{GS}} = f_F(vL^{z+1/\nu}), \quad (23)$$

by simply graphing $-\log F_{\text{GS}}$ versus $x = vL^{z+1/\nu}$, as we do in Fig. 20(a) for the case of QA to the critical point s_c . There are no adjustable parameters and the data exhibit surprisingly good data collapse, considering the small system sizes. In the limit of small values of x , the scaling function $f_F(x)$ onto which the data collapse takes the form $f_F \sim x^2$. This behavior is expected from adiabatic perturbation theory (APT) [49, 50], which applies in the low-velocity limit of finite systems because of their critical gaps $\Delta(L) \propto L^{-z} = L^{-1}$. APT predicts a v^2 behavior, multiplied by a power of L compatible with KZ scaling. The fact that $x \propto v$, implies the observed quadratic behavior in x .

In Fig. 20(a), the data for each system size deviate from the common scaling function in the high-velocity

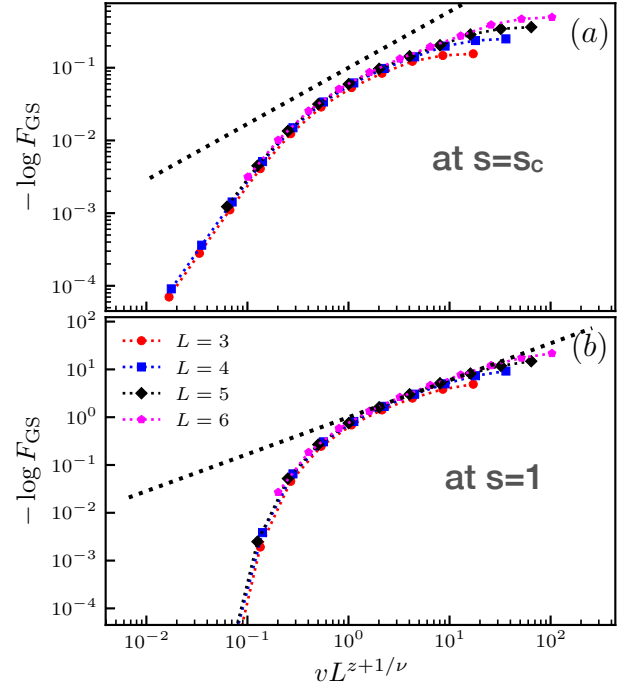


FIG. 20. Log fidelity at the infinite-size critical point s_c in (a) and in the classical limit $s = 1$ in (b). The annealing velocity v has been scaled with the KZ time $L^{z+1/\nu}$ with $z = 1$ and $1/\nu = 1.587375$. The lines have the slopes expected at large $x = vL^{z+1/\nu}$ for a system exhibiting KZ scaling.

limit, where the $v \rightarrow \infty$ value for given L corresponds to the overlap between the critical state and the trivial initial state. This overlap of course decreases with increasing L , but a KZ scaling regime gradually builds up as L increases, with the high- v crossover shifted to larger values of x . The log fidelity here is expected to be proportional to L^d [50, 51, 92], which corresponds to the ground state probability being exponentially small, $F_{\text{GS}} \sim \exp[-a(L/\xi_v)^d]$ with a velocity independent a . The scaling form Eq. (23) then implies $f_F \rightarrow (vL^{z+1/\nu})^{d/(z+1/\nu)}$, which is indicated by the dashed line in Fig. 20(a). Here the match with the data is not perfect but appears to improve slowly with increasing system size. The plausibility of the slow approach is supported by the fact that the finite-size critical points, which can be taken as the t/T_{\max} point of the maximum value of $-\log F_{\text{GS}}$ in data such as in Fig. 19, are still quite far away from the $L \rightarrow \infty$ critical point for the small system sizes considered here.

The regime of asymptotic power law should formally correspond to $1 \ll \xi_v \ll L$ and large L , which is commonly referred to as the KZ scaling regime. However, it should again be noted that the KZ time scale $L^{z+1/\nu}$ also applies when $L < \xi_v$, where the QA process for finite L approaches fully adiabatic. The entire regime $\xi_v \gg 1$ is therefore governed by the finite-size KZ mechanism. Despite the finite-size corrections to the scaling function in Fig. 20(a), the fact that the data do collapse versus

$vL^{z+1/\nu}$ both in the near-adiabatic and KZ regimes is quite remarkable, given the small system sizes. To improve the data collapse in the KZ scaling regime, the maximum values of $-\log F_{\text{GS}}$, the locations of which can be taken as $s_c(L)$ [and are seen to drift toward $s_c = s_c(\infty)$ Fig. 19] can in principle be used instead of the $s = s_c$ values in Fig. 20(a). This procedure removes some of the subleading finite-size corrections stemming from the drift of $s_c(L)$. Even more impressive is that the log fidelity at the final point $s = 1$, analyzed in Fig. 20(b), exhibits almost perfect KZ scaling, not just with excellent data collapse overall but also reproducing the expected asymptotic power-law form with much less finite-size corrections than at s_c . Thus, while there is a steep increase and rather complicated oscillations in $-\log F_{\text{GS}}$ close to the quantum phase transitions, as seen in Fig. 19, the behavior once the oscillations have decayed away reflects a very stable probability of the system to remain in the ground state after traversing the critical point.

The asymptotic behavior for $x \rightarrow 0$ in Fig. 20(b) is a much faster approach to 0 than the x^2 form at the critical point in Fig. 20(a), thus showing that a large fraction of the defects produced in the neighborhood of the critical point are removed in the QA process continuing into the ordered phase (though with the size dependence $L^{z+1/\nu}$ of the overall time scale maintained), as is also reflected in the decay of $-\log F_{\text{GS}}$ after the large maximum in Fig. 19. The asymptotic $x \rightarrow 0$ behavior seems to be exponential but we have not analyzed the form further.

KZ scaling deep inside the ordered phase is not expected in most observables but is unique to the gap-protected post-critical ground-state probability (and directly related quantities). As we will see below in Sec. IIIB, observables that depend also on the properties of the evolved excited states exhibit very different scaling behaviors, originating in coarsening processes similar to those in the classical model under SA. We therefore do not test for KZ scaling at $s = 1$ of the observables defined in Eqs. (19). As for KZ scaling of these observables at s_c , results are shown in Fig. 21 with vertical scaling of each quantity according to the scaling dimensions discussed previously. In the case of the energies, we have subtracted their respective size dependent equilibrium values, i.e., we study the excess energies. Like the log fidelity, in all cases the data collapse is almost perfect without any adjustable parameters but the asymptotic power-law behavior of the scaling function are again not yet fully manifested, though evolving slowly in the right direction with increasing L . In the case of the squared magnetization in Fig. 21(a), the asymptotic slope is already almost reproduced.

The asymptotic forms for large x (and large L) are again obtained from the KZ scaling ansatz Eq. (4) by requiring the trivial L dependence (with a resulting corresponding v dependence) of the observables in the limit where $\xi_v \ll L$ [53], which in the case of the squared sublattice magnetization is $m^2 \sim L^{-d}$ while the energy densities are L independent. While the limit $1 \ll \xi_v \ll L$

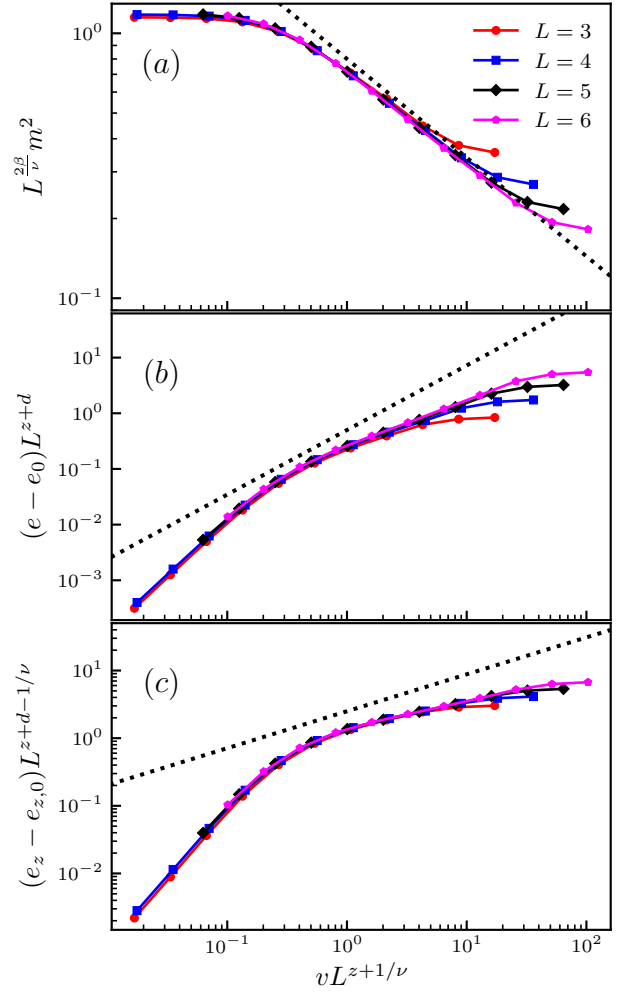


FIG. 21. Finite-size KZ scaling collapse for the squared order parameter (a), the excess total energy density (b), and the excess Ising energy density (c). The critical exponents ν and β used in this plot correspond to their known 3D Ising values and $z = 1$. The dashed black lines in each of the panels correspond to the asymptotic KZ power-law behavior for large $vL^{z+1/\nu}$ when $L \rightarrow \infty$.

in which the KZ scaling function $f(x)$ takes its large- x limiting form of a power law in x may seem formally impossible to realize with system sizes only up to $L = 6$, in practice, as we have seen, we still observe almost the correct KZ power laws in Fig. 21. The overall KZ time scale $L^{z+1/\nu}$ is also realized there and in the near-adiabatic $L \ll \xi_v$ regime. Our interpretation of this surprisingly good scaling for small systems is that the subleading finite-size corrections are small in the near-adiabatic regime $L \ll \xi_v$ and the crossover to the KZ power laws is fast (as manifested in the rather sudden changes in slopes in Figs. 20 and 21). The only minor deviations from the KZ power laws show that the corrections are small also when $L \gg \xi_v$ is not fully realized.

In the adiabatic limit, $m^2 L^{2\beta/\nu}$ approaches a constant at s_c , as is clearly seen in Fig. 21(a); the approach to the constant form should be analytic, given that the generic

scaling function $f(x)$ in the KZ scaling form Eq. (4) is analytic in x . To analyze the the adiabatic limits of the excess energies, we have to take into account that the equilibrium finite-size energies have been subtracted off in Fig. 21, while the original generic KZ form Eq. (4) (with κ/ν replaced by Δ_e or Δ_{e_z}) assumes that the excess is defined with respect to the thermodynamic limit (i.e., the scaling is for the combined effects of finite size and finite velocity at the critical point). The subtracted finite-size equilibrium energy simply corresponds to removing the constant term in the scaling function, i.e., with the example of the total energy density,

$$L^{\Delta_e}[e(L, v) - e(L, 0)] = f_e(vL^{1/\nu}) - f_e(0) \quad (24a)$$

$$= g_e(vL^{1/\nu}) \propto (vL^{1/\nu})^a + \dots, \quad (24b)$$

where we have defined a new scaling function $g_e(x)$ with asymptotic form x^a , with the integer valued exponent $a \geq 1$ representing the leading non-adiabatic corrections. Similarly, we can define g_{e_z} for the excess Ising energy. The question then is what the leading exponents a are for these excess energies.

As we are dealing with finite systems that always have nonzero instantaneous gaps, APT can again be applied [49, 50]. When stopping at the critical point, if the observable commutes with $H(t)$ at the time of measurement, then the leading-order correction to the adiabatic limit should be quadratic in v , which obviously applies to the total excess energy $e - e_0$ (and also the case of the log fidelity analyzed in Sec. III A). In other cases the dependence is in general linear in v . However, the constant of proportionality is the Berry curvature, which vanishes unless the operator (or the Hamiltonian itself) breaks time-reversal symmetry [51]. The Ising energy being time-reversal symmetric, we also expect a quadratic v dependence for $e_z - e_{z,0}$ (unlike the case of imaginary time QA, where the constant is the metric tensor, which does not vanish and the low- v form is linear [50, 51]). For both energies, powers of the system size multiply the v^2 dependence. Since the KZ scaling functions $g_e(x)$ and $g_{e_z}(x)$ must obey the limiting near-adiabatic power laws when $x \rightarrow 0$ and $x \propto v$, we should simply have $g_e(x) \sim x^2$ and $g_{e_z}(x) \sim x^2$, both of which are indeed reproduced essentially perfectly by the data in Fig. 21(b) and Fig. 21(c).

B. Ordering kinetics and defects

KZ scaling provides a generic framework for understanding QA ending at a quantum-critical point, and generalizations applying at the initial stages of entering an ordered phase have also been proposed [17, 41, 45]. Much less is known in general about the dynamics that ensues when annealing deep into the ordered phase. It is commonly understood that the excitations created at the critical point “freeze out” in the ordered phase, in which case KZ scaling would apply all the way to the classical limit of the QA protocol. Indeed, in cases where all

kinetic ordering processes are much slower than the critical fluctuations governing KZ scaling, the final classical state will to a high degree reflect the critical state. Such a “memory” of the critical state has been observed in QA annealing of programmable spin glasses in D-Wave devices [17, 18]. Extremely slow dynamics of random in systems corresponding to hard optimization problems (e.g., spin glasses) should in general be due to a phenomenon similar to Anderson localization that is associated with a high density of exponentially small gaps in the ordered (or glass-type) phase [95]. In contrast, as observed in Sec. II A, and previously with less detail in Ref. [36], much faster coarsening dynamics and interface fluctuations take over when crossing into the ordered phase in classical SA of the uniform 2D ferromagnet. The emergence of similar faster ordering processes beyond the KZ mechanisms should also be expected in QA of uniform quantum system (and perhaps in many disordered ones as well) [37, 40, 41].

In the case of QA of the Ising model, the most plausible fast ordering mechanism (which is also supported by our study) is thermalization of the gap-protected excitations in the ordered phase [38, 65, 66], with the essentially conserved excess energy supplied to the system when crossing the phase transition. However, the lack of reliable numerical methods (and, as our work demonstrates, the neglect so far of small systems) in dimensions higher than one has inhibited unbiased computational progress on the late-time QA dynamics. Calculations have been largely restricted to mean-field models [68, 70], field-theory analysis [38], large- N approximations [93, 94], and models that map to free fermions [15, 28–33, 68, 71, 72]. Some of these works have demonstrated domains formed by coarsening dynamics [38, 94], while in other works it was argued that the domain sizes are predicted by the Landau-Zener approximation of annealing [29, 68, 70].

Similar to the SA case discussed in Sec. II A, we are here interested in the types of domains that form at the end of the QA protocol and their associated time scales of elimination. We will investigate the squared order parameter and the Ising energy density (which at $s = 1$ is the same as the total energy density) and test whether these quantities obey the same type of scaling form as in the SA case, Eqs. (9). We also develop methods to specifically probe the excited states, which allows better access to the rare system-spanning topological defects that remain at the end of slow QA processes.

To first test for coarsening dynamics with the same exponent $\alpha = 2$ as in classical SA, in Fig. 22 we plot m^2 and $L(e_z - e_{z,0})$ against vL^2 , as previously in the case of SA in Figs. 3(c) and 4(b). Both quantities show a very good scaling collapse, indicating that $\alpha = 2$ is most likely the correct power-law relationship between the domain size and time scale in this velocity regime. In the regime where the velocity-limited correlation length is significantly smaller than the system size, $\xi_v \ll L$ [where now ξ_v does not follow the KZ form Eq. (2) since the QA process is no longer in the vicinity of the critical point],

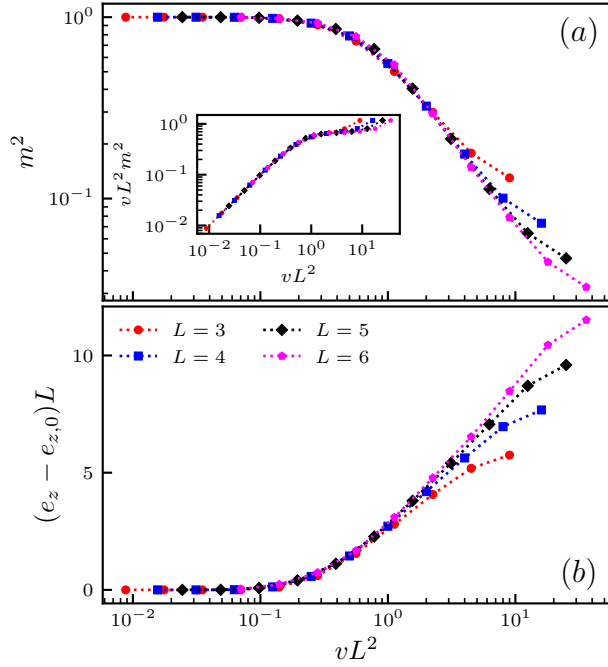


FIG. 22. Scaling at $s = 1$ of the squared order parameter (a) and the excess Ising energy density multiplied by L (b), both vs vL^2 . The observed data collapse when scaling the velocity by L^2 corresponds to ordering by coarsening dynamics of confined defect domains.

the squared order parameter must scale as $m^2 \sim 1/L^2$. This regime should correspond to Fig. 22(a) where the collapsed data fall on a straight line on the log-log plot. In the coarsening form $m^2 = f_m(vL^2)$ the scaling function must have the limiting behavior $f_m(x) \sim 1/x$ for large x , provided that both $x = vL^2$ and L are large enough. The asymptotic form is demonstrated in the inset of Fig. 22(a) with $m^2(x)$ multiplied by x so that a constant behavior should apply for large x . While the data for each L peels off from the approximately flat portion of the almost collapsed function, the deviations are pushed to larger x with increasing L and the plateau also becomes more flat.

The size independence of $L^2 m^2$ in a disordered system with finite correlation length also of course must apply in the KZ scaling regime with $L \gg \xi_v$ (now with ξ_v taking the KZ form), which we return to momentarily to contrast the KZ and coarsening behaviors. In Fig. 23 we graph the inverse-velocity dependence of $L^2 m^2$ both at s_c , in Fig. 23(a), and at $s = 1$ in Fig. 23(b), along with the expected power-law forms. At s_c the exponent a in $L^2 m^2 = (1/v)^a$ is obtained from KZ scaling by demanding $m^2 L^2 = L^{2+2\beta/\nu} (vL^{z+1/\nu})^a$ to be L independent, which gives $a = 0.4267$. This KZ scaling regime is manifested in Fig. 23(a) versus $1/v$ instead of $vL^{z+1/\nu}$ used in Fig. 21(a). Now there is data collapse also in the high-velocity regime (not in the near-adiabatic low-velocity regime) and the crossover to KZ scaling also happens rather abruptly (like the crossover between KZ

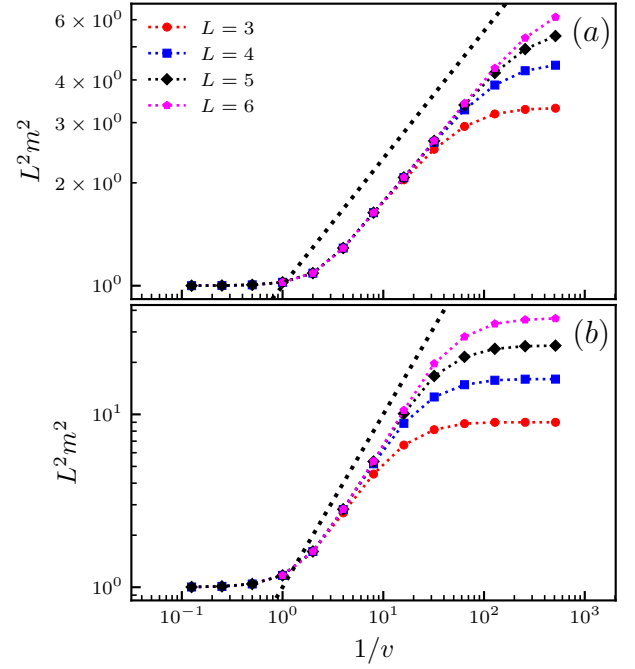


FIG. 23. The squared magnetization scaled by the system volume, graphed vs the inverse QA velocity so that collapse onto a common scaling function should take place in the high-velocity limit as well as (a) in the KZ scaling regime for a process measured at s_c and (b) in the coarsening regime when measuring at $s = 1$. The dashed line in (a) shows the slope expected (the line being offset from the data for clarity) in the KZ regime, $f(1/v) \propto (1/v)^{0.4267}$. In (b) the slope of the dashed line corresponds to the stage of coarsening when the domains are still of size $l \sim L$, where $f(1/v) \propto 1/v$. In both cases, there is no collapse to a common scaling function for large $1/v$, where the systems are nearly adiabatic and the data in (a) and (b) instead collapse when graphing as in Fig. 21(a) and Fig. 22(a), respectively.

and near-adiabatic forms in Fig. 21), with only very small corrections. The asymptotic KZ power-law behavior that should be attained for large $1/v$ and large L is again observed with almost the expected exponent for the largest system and the correct trend of improving with increasing L is clear. Returning to $s = 1$, here we obtain a very different exponent $a = 1$ from demanding the L independence of $L^2 m^2 = L^2 (vL^2)^a$. The $1/v$ form is indeed closely realized in Fig. 23(b) and the slope again improves with increasing L . While the results in Figs. 23(a) and 23(b) are not fully converged to their large- L and large- $1/v$ forms, they clearly support and contrast the respective KZ and coarsening regimes.

Unlike the case of classical SA, the data collapse versus vL^2 in Fig. 22 seems to apply all the way down to the limit of saturated long range order, without the crossover to the L^3 (or other power of L) scaling seen in the SA results in Figs. 3 and 4. We can nevertheless confirm that horizontal and vertical system-spanning domains are prevalent in late-stage QA as well and are associated with the same L^3 time scale as in SA. We will also show that

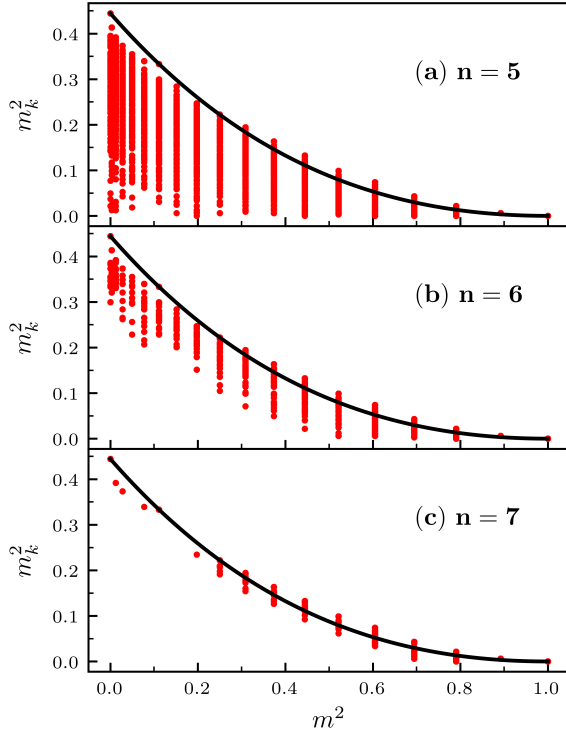


FIG. 24. Scatter plots in the plane of the conventional order parameter m^2 and the stripe defect order parameter m_k^2 , Eq. (11), based on 10^5 spin configurations sampled from the $s = 1$ wave function after QA of an $L = 6$ system. Panels (a), (b), and (c) correspond to annealing velocities, $v = 2^{-n}$, with $n = 5, 6$, and 7 , respectively. The black curve in all three panels indicates the function Eq. (14) of m_k^2 vs m^2 for perfectly straight stripe domains in the system. Note the very limited number of different m^2 values for this small system size, while there are significantly more allowed values for m_k^2 .

their effects on the order parameter and excess energy are small on the scales used in Fig. 22 but that they can be observed clearly when analyzing the data in other ways.

First, to confirm the relatively longer time of persistence of the large-scale domains, in Fig. 24 we show a scatter plot analogous to the classical Fig. 8, with the long-wavelength domain order parameter m_k^2 defined in Eq. (11) graphed versus the conventional squared order parameter. Here we have sampled 10^5 spin configurations from the final $s = 1$ QA wave function for the $L = 6$ system after annealing at three different velocities. Even though the resolution here is limited by the small system size (i.e., a small number of accessible values of the two quantities, with many spin configurations giving the same values), at the lowest velocity the accumulation of instances of (m^2, m_k^2) around the curve Eq. (14) corresponding to smooth straight domains (which is not a strict upper bound for finite L) confirm the configurations at this velocity are essentially all either fully ferromagnetic, corresponding to the majority of configurations at $(m^2, m_k^2) = (1, 0)$, or contain one stripe domain. Note that, in this case the probability of (m^2, m_k^2) falling close to $(0, 0)$ is extremely small (unlike the classical re-

sults in Fig. 8), with not a single sampled configuration seen in this region in Figs. 24(b) and 24(c). Thus, diagonal domains in the late stage QA process are very rare for the small systems considered here. Indeed, looking at the pictorial representations of spin configurations with winding number $W = (1, 1)$ in Fig. 2(c), it is clear that there is essentially no room in periodic lattices of size $L \leq 6$ to accommodate diagonal domains.

The presence of the horizontal and vertical stripe domains can also be detected in m^2 and e_z by analyzing the approach to their asymptotic values in more detail than in Fig. 23. Here we can take advantage of the fact that the numerical solution of the Schrödinger equation delivers the exact probability amplitude of the two classical ground states (i.e., the fidelity discussed in Sec. III A). We here define $|a_0|^2$ as the sum of the probabilities of the two fully ferromagnetic states. Given that $m^2 = 1$ and $e_z = -2$ are also trivially known in these states, by subtracting $|a_0|^2$ and $-2|a_0|^2$, respectively, from the $s = 1$ values of m^2 and e_z we can analyze the contributions stemming specifically from the excited states. Conjecturing that the time scale of elimination of the stripe domains is $\propto L^3$, as in classical SA according to the results in Sec. II A, in Fig. 25 we graph results versus $x = vL^3$. Here there is no further rescaling of the results by powers of L , because there are only small (of order-one size) confined domains left when the stripe domains have been eliminated. The fact that the data for small x in Fig. 25 indeed collapse onto a very fast decaying function for small x confirm this scenario of a time $\propto L^3$ required before the remaining defects are all very small.

We can further divide the quantities in Fig. 26 by the probability $1 - |a_0|^2$ of the system being in any of the excited states. The asymptotic low-velocity forms should then correspond to the properties of the first excited state of the classical Ising model, which has total energy $E_z = Ne_z = -2N + 8$ and total squared magnetization $M^2 = N^2 m^2 = (N - 2)^2$. Accordingly, we define quantities representing positive deviations from these values:

$$\Delta_M = (N - 2)^2 - \frac{N^2(m^2 - |a_0|^2)}{1 - |a_0|^2}, \quad (25a)$$

$$\Delta_E = \frac{N(e_z + 2|a_0|^2)}{1 - |a_0|^2} + 2N - 8. \quad (25b)$$

Results are shown in Fig. 26 versus $x = vL^3$. In the case of Δ_M , in order to achieve data collapse for small x , the results also have to be divided by (essentially) the system volume, which is simply explained by the fact that the total magnetization $|M|$ here is a quantity deviating only by a small amount δ from $N - 2$. With $(N - 2 - \delta)^2 = (N - 2)^2 - 2(N - 2)\delta - \delta^2$, the $(N - 2)^2$ term is eliminated in Eq. (25a) and the remaining leading term $(N - 2)\delta$ is dealt with by dividing out $N - 2$ in Fig. 26(a). The δ^2 term is not important. The data for both $\Delta_M/(L^2 - 2)$ and Δ_E , the latter with no rescaling in Fig. 26(b), clearly approach common scaling functions $f_{M,E}(vL^3)$ for increasing L .

Since the results in Fig. 26 represent small differences

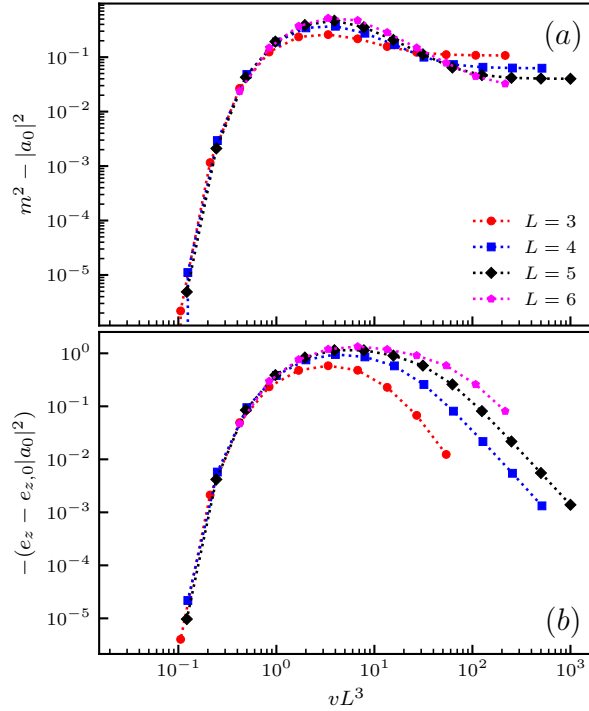


FIG. 25. Squared sublattice magnetization (a) and Ising energy (b) after QA to the classical limit $s = 1$ with the contributions from the two fully ferromagnetic ground states subtracted off. The results are graphed vs $x = vL^3$, corresponding to the conjectured time scale of elimination of system-spanning stripe domains. When these domains have been eliminated, for sufficiently small x , the remaining excitations only contain confined domains of order-one size, which is here reflected in the lack of vertical rescaling in both (a) and (b).

of large numbers as per Eq. (25), they are more sensitive to numerical integration errors than the conventional quantities analyzed previously. These errors become apparent for the longest integration times and (smallest values of the computed differences) and in Fig. 26 we therefore only show results for those velocities for which no numerical anomalies are apparent. There is still a significant range of points for small vL^3 for which the data collapse for $L = 4, 5$, and 6 is satisfying and clearly improves with increasing system size. We conclude that the time scale L^3 is detectable in QA and that it arises from straight stripe domains, as evidenced also by the more qualitative results in Fig. 24.

By scaling the same data as in Fig. 26 under the assumption that the system still hosts domain walls of length $\propto L$, i.e., at times before the ultimate convergence of the excitations to those of the lowest energy, we can also recover the conventional coarsening time scale L^2 , as shown in Fig. 27. Here the presence of large defect domains, whether confined or system-spanning, corresponds to both terms in Eq. (25a) being of order N^2 but not close to canceling each other (in contrast to the other limit considered above). Thus, for scaling we should normalize Δ_M by $(N - 2)^2$, as we do in Fig. 27(a) when

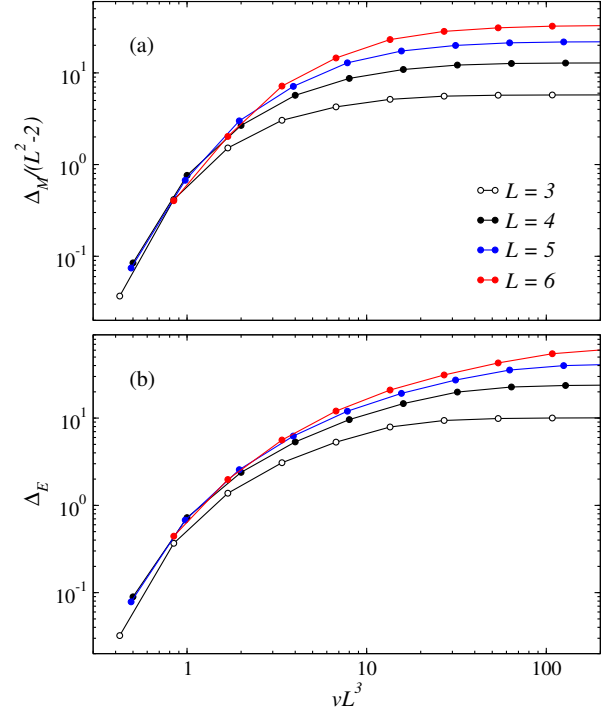


FIG. 26. The contributions from excited states to (a) the squared magnetization and (b) the total Ising energy, with the corresponding values of the observables in the lowest excited state subtracted off, as precisely defined in Eqs. (25). The scaling of the velocity by L^3 corresponds to the conjectured time for elimination of stripe domains. The results in (a) have been further rescaled by dividing with the system volume minus 2 (the absolute value of M in the lowest excited state), as discussed in the text.

graphing versus $x = vL^2$. For $x \gtrsim 0.5$, the data for $L = 4, 5$, and 6 collapse almost perfectly onto a common function, and the tendency to collapse also for small values of x clearly improves with increasing L .

In the case of Δ_E , the assumption of remaining large defect domains suggests that $\Delta_E \propto L$ should be analyzed, as we do in Fig. 27(b). Here the data collapse is not quite as good as in Fig. 27(a), but still clearly improving with increasing L . Note that both quantities in Fig. 27 exhibit the poorest data collapse for the smallest x values for all L , because those are in the velocity regime where the large-scale defects have vanished and the results instead show better scaling in Fig. 26. However, even at the smallest values of vL^2 , the deviations from the emergent scaling function are not very large, though the same data sets collapse very well in Fig. 26. Thus, these low-velocity results for small systems are still in a regime where the time scales L^2 and L^3 cannot be clearly separated when graphing on a larger scale, as in Fig. 22, thus explaining the lack of visible deviations from conventional coarsening behavior in said graph. Data for smaller vL^3 would be useful in order to extend the range of good data collapse in Fig. 26, and, conversely, to see larger deviations from a common scaling function for small vL^2 and small

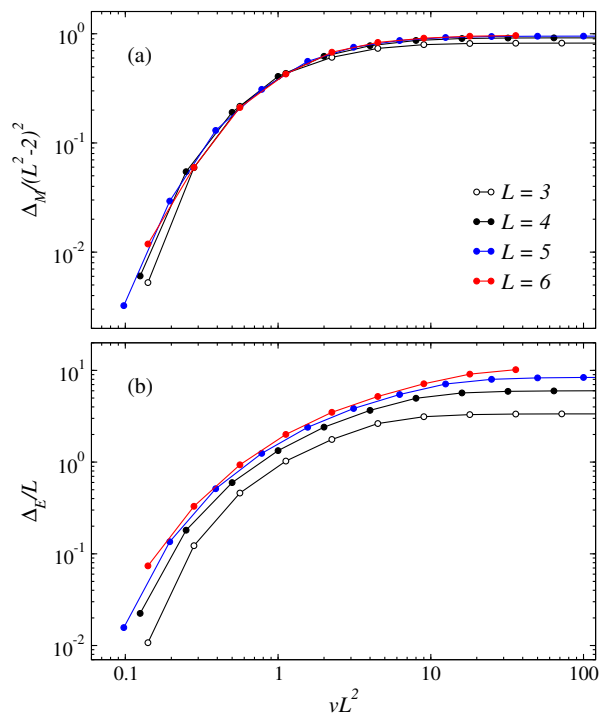


FIG. 27. The data from Fig. 26 graphed versus νL^2 , with a rescaling of Δ_M by $1/(L^2 - 2)^2$ in (a) and of Δ_E in (b) by $1/L$, for reasons discussed in the text.

L in Fig. 27, but this would require an even more stringent convergence criteria for the demanding long-time numerical solutions of the Schrödinger equation.

IV. CONCLUSIONS AND OUTLOOK

In this paper we first investigated the final-stage $T \rightarrow 0$ ordering kinetics in SA of the classical Ising model and then used insights gained there to analyze the limit of vanishing transverse field in QA of the corresponding quantum model (TFIM) with a transverse field. The primary difference in focus from previous SA [36] and numerical QA [45] works on the same model is the role played by system-spanning topological defects. The original ideas of KZ concerned exactly the slow dynamics of large-scale defects, in the universe [26] and in liquid ^4He [27], but later works on SA and QA have largely neglected them—or, in the case of QA, involved 1D systems in which the domain walls are point-like and less interesting. Even in the context of classical phase-ordering kinetics [34], the focus has normally been on the growth of domains by coarsening at finite temperature in the thermodynamic limit, while we here have studied in detail how both confined and system-spanning minority domains eventually are eliminated in finite systems under SA and QA.

In SA on periodic lattices (in which domain walls can be classified by the topological winding number), hori-

zontal and vertical stripe defects vanish on a time scale L^3 , while diagonal domains have the longer life time $\propto L^{z+1/\nu} \approx L^{3.17}$ corresponding to the KZ mechanism. With open boundaries, the formal distinction between different types of system-spanning domain walls no longer applies (the winding number is not defined) and only the L^3 scale is manifested for all system spanning defects at the $T = 0$ end point of the SA process. The time scales of elimination of system-spanning stripe defects again exceed the L^2 scale of conventional coarsening dynamics, which we also observed in the open systems using finite-size and -velocity scaling.

The L^3 time scale of elimination of system-spanning domain walls in the 2D classical Ising model was found and partially explained some time ago in MC simulations at fixed temperature $T < T_c$ [63], and was further elucidated in the context of sudden quenches to $T = 0$ of random states [59, 60, 62]. Some of our SA results clearly connect to these previous findings. However, in SA there is the further interesting and complicating aspect of interplay between the KZ mechanism and ordering kinetics when the system is annealed slowly past a critical point into the ordered phase. The time scale $L^{3.42}$ of elimination of diagonal domains in periodic systems at fixed $T < T_c$ (where the exponent represents an improvement over a previous estimate [59]) is longer than the KZ scale of remaining in equilibrium when traversing the phase transition. This fact explains why the prevalence of diagonal domains is actually, as mentioned above, controlled by the KZ exponents even for SA all the way to $T = 0$, in clear analogy with the original KZ ideas of “frozen” topological defects. However, since the horizontal and vertical domain walls are eliminated on a shorter time scale in the 2D Ising model below T_c , they do not obey KZ scaling in SA into the ordered phase. Moreover, since diagonal domain walls are not well defined in open systems, the longer time scale associated with them is absent there, and it appears that no physical observables obey KZ scaling in SA to $T = 0$ unless periodic boundary conditions are applied. The important role of the slow dynamics of system-spanning domain walls carries over to QA as well, where the L^3 time scale that we confirm for straight domain walls also in this case is slower than the KZ scale $L^{2.59}$ and, therefore, the survival probability of these domains should actually obey KZ scaling in QA all the way to the classical limit (vanishing field), with periodic as well as open boundary conditions.

While our exact numerical QA calculations were limited to very small periodic $L \times L$ lattices with $L \leq 6$, the results exhibit remarkably good scaling. We confirmed KZ scaling of the ground state fidelity, which is protected by the gap in the ordered phase, even in the extreme limit of QA to vanishing field. Other quantities like the excess energy and the order parameter exhibit KZ scaling at the critical field, while in the ordered phase the time scale L^2 of quantum coarsening is seen very clearly. Though the time scale L^3 of elimination of horizontal and vertical stripe domains is not easily observed in conventional ex-

pectation values, we were nevertheless able to detect this time scale by isolating the contributions from the excited states, which are not subject to KZ scaling (other than in their overall collective probability) because of their gapless spectrum when $L \rightarrow \infty$.

It may appear surprising that systems of size $L \leq 6$ can realize all these scaling behaviors—with three different times scales detected—especially in light of the fact that much larger systems are required to achieve good scaling in SA. It should be kept in mind, however, that the quantum system is effectively 2+1 dimensional when mapped to a classical problem, and it should therefore be more appropriate to judge the size of the system in terms of its space-time volume, where the velocity-limited correlation length ξ_v should correspond to the length in the time direction. In the related problem of eigenstate thermalization, small systems were also sufficient for drawing conclusions about the thermodynamic limit [96–98].

All our QA results in the ordered phase point to the same ordering mechanisms as in SA, though with the twist that the KZ exponents are different and this affects the way in which the different times scales of ordering kinetics can be observed. Coarsening dynamics of classical systems has also previously motivated proposals for emergent classical hydrodynamic descriptions of quantum systems obeying eigenstate thermalization hypothesis [86, 90, 91]. The main idea here is that energy is pumped into the system when it crosses the phase transition, with subsequent relaxation of the excitations to a finite-temperature state (in which the ground-state probability does not obey Gibbs statistics because it is essentially conserved after traversing the critical point) for a sufficiently slow QA process. If the resulting temperature is lower than the critical temperature, the system will equilibrate and begin to form larger domain walls (coarsen), while at higher temperature the system remains disordered [37, 38].

This idea of emergent classical hydrodynamics by thermalization of excitations has been checked in various semi-classical works on sudden quenches [39, 93] and ramps [94], but, to our knowledge, exact numerical results like those obtained here for a fully quantum mechanical 2D system have not been presented before. The closest case is Ref. [45], which used sophisticated many-body methods for larger system sizes and found signs of coarsening dynamics. However, due to limitations on the annealing time it was not possible to continue the QA process deep into the ordered phase and observe the L^2 time scale. The fate of the extended domain walls that we have emphasized here was not addressed. A quantum MC method based on the time dependent variational principle [84, 85] was previously applied [86] to the same TFIM, but the focus there was on thermalization and the specifics of critical and ordering dynamics were not addressed. The fact that we also observe the same L^3 time scale as in SA for elimination of system-spanning defects is a further indication of thermalization and emergent classical ordering kinetics in QA.

While our QA study of the TFIM gives a fairly complete picture of the different types of defects and their associated time scales in critical and ordering dynamics, there are still remaining issues beyond the reach of the exact solutions of small systems employed here. In particular, it would be interesting to study both straight and diagonal stripe domains more completely in QA, using the winding number methods that we employed in the context of classical SA. An interesting prospect is that experimental QA platforms may be superior to classical calculations in this regard. Both D-Wave quantum annealers and Rydberg atom arrays should be suitable for this purpose. In the former, measurements can currently be performed only in the final annealed state at $\Gamma = 0$ [17, 18]. This limitation is no disadvantage in the present context, which concerns exactly the final QA stage. It is also not necessary here to strive for very large system sizes, given that already $L \leq 6$ results show good scaling. It would be very interesting to experimentally test the L^3 time scale of survival of horizontal and vertical stripe domains in larger systems, as we have done here already with the small lattices in various ways. It is noteworthy that this time scale is also present in systems with open boundary conditions, which are easier to implement in practice. Analyzing the surviving system-spanning domains in periodic systems of size $L = 10 \sim 20$ would likely also resolve the outstanding issue of the time-scale of diagonal stripe domains. Currently, fully periodic lattices of native qubits can be studied with D-Wave annealers for $L \leq 12$ [19]. D-Wave devices may also have an advantage here in terms of their short annealing times possible with the relatively large energy scales of the coupled qubits and efficient state preparation and measurements. This aspect is important, as a large number of repetitions of the QA process will be required in order to collect sufficient statistics.

Our main specific prediction for QA of the TFIM to $\Gamma = 0$ are: (i) The probability P_{GS} of reaching one of the fully ferromagnetic ground states should obey KZ scaling, i.e., $P_{\text{GS}} = f(vL^{z+1/\nu})$ with $z + 1/\nu \approx 2.59$. (ii) The probability of observing any system-spanning domain wall should also obey KZ scaling. (iii) The longer time scales of order L^3 (for horizontal and vertical domain walls in both periodic and open systems) and $L^{3.42}$ (conjectured for diagonal domains in periodic systems) should be manifested in statistical measurements including the excited states only, i.e., all instances of QA which do not lead to one of the fully ferromagnetic ground states. Sufficiently long annealing times will be required in order to eliminate most confined defects by coarsening and to establish non-fractal domain walls; otherwise the conventional coarsening processes will dominate the measurements. The longer time scale of the diagonal domains in periodic systems will also be more difficult to detect because the horizontal and vertical domains are more prevalent.

While the best way to detect the time scales of system-spanning defects should be to count them explicitly in the

measured QA configurations, conventional physical observables, like the order parameter and the energy should also be useful in this regard. In experiments, when averaged over the classical excited states only, Eqs. (26) for the differences with respect to the lowest excited states can be written more conveniently as just

$$\Delta_M = (N - 2)^2 - M^2 \quad (26a)$$

$$\Delta_E = E_z + 2N - 8, \quad (26b)$$

where M is the total magnetization (not divided by the volume) and E_z the total Ising energy. Here Eq. (26b) applies for periodic boundary conditions, while for open systems the energy cost of the smallest local defect should be replaced by 4, i.e., the energy of a corner defect. Similarly, for cylindrical boundary conditions the lowest excitation energy, that of a flipped spin on one of the open edges, is 6. The quantities Δ_M and Δ_E should be analyzed as in Fig. 26 to detect the both the times scales L^3 and $L^{3.42}$ (which should multiply v on the x axis) and as in Fig. 27 to detect the coarsening time $\propto L^2$.

Beyond the prospect of using QA devices to resolve outstanding issues for one of the prototypical quantum many-body systems, the presence of three different times scales in QA of the TFIM also provides an opportunity to define a rigorous experimental test-bed. In particular, break-down of scaling at long annealing times is expected due to finite temperature and, possibly, other noise effects [13, 15, 17, 99, 100]. It will be useful to observe the exact manifestations of these imperfections in the different types of critical scaling and defect elimination that we have discussed here. For small systems, minor randomness in the couplings will likely be less important (while eventually becoming important for large systems). The 1D TFIM also is an excellent model for such tests [15], but the 2D case has much richer scaling behavior, as we have seen, with clear differences between KZ scaling and ordering kinetics.

It is not clear to us how capable current devices would be to test our predictions (i)–(iii) above, but experiments on the 2D ferromagnet with a previous generation of the D-Wave device [13], as well as more recent D-Wave ex-

periments on 1D systems [15] and spin glasses [17, 18], suggest that at least the coarsening scale L^2 and the KZ scale $L^{2.59}$ should be detectable at the time scales before the noise effects become important with this platform. Recent D-Wave experiments with other models implemented have already observed some aspects of coarsening [16], as have experiments with Rydberg atoms [24]. The scaling approaches we have developed here should help to more clearly observe the time scale of coarsening with current and future devices, and it will of course be particularly interesting to test our predictions for system-spanning domain walls.

The results presented here also pose a constructive challenge for recently improved tensor-network [46] and neural-network [47] methods, which were claimed to simulate even complex 3D spin-glass QA problems more efficiently than in recent work [17, 18] with D-Wave annealers. These claims have themselves been countered [101], with the main point of contention being whether the classical calculations for small system sizes (tens of qubits) and short times can really be extended with maintained fidelity to systems orders of magnitude larger (hundreds to thousands of qubits in the experiments) and much longer annealing times. The uniform ferromagnetic 2D TFIM might appear to be a much easier problem for the new algorithms, but it may still be challenging to reach the long time scales on which system-spanning defects are formed when crossing the phase transition and subsequently decay away in the ordered phase.

ACKNOWLEDGMENTS

We would like to thank Mohammad Amin, Anushya Chandran, Leticia Cugliandolo, Andrew King, Paul Krapivsky, Pranay Patel, Anatoli Polkovnikov, and Jack Raymond for interesting and helpful discussions. This work was supported by the Simons Foundation under Grant No. 511064. The calculations were carried out on the Shared Computing Cluster managed by Boston University's Research Computing Services. The numerical solutions of the Schrödinger equation were obtained using the QuSpin library [102].

-
- [1] S. Kirkpatrick, C. D. Gelatt, Jr., and M. P. Vecchi, Optimization by Simulated Annealing, *Science* **220**, 671 (1983).
 - [2] V. Černý, Thermodynamical approach to the traveling salesman problem: An efficient simulation algorithm, *J. Optim. Theor. and Appl.* **45**, 41 (1985).
 - [3] V. Granville, M. Krivanek, and J.-P. Rasson, Simulated Annealing: A Proof of Convergence, *IEEE Trans. Pattern Anal. Mach. Intell.*, **16** 652 (1994).
 - [4] A. B. Finnila, M. A. Gomez, C. Sebenik, C. Stenson and D. J. Doll, Quantum annealing: A new method for minimizing multidimensional functions, *Chem. Phys. Lett.* **219**, 343 (1994).
 - [5] T. Kadowaki and H. Nishimori, Quantum annealing in the transverse Ising model, *Phys. Rev. E* **58**, 5355 (1998).
 - [6] D. Bitko, T. F. Rosenbaum, and G. Aeppli, Quantum Critical Behavior for a Model Magnet, *Phys. Rev. Lett.* **77**, 940 (1996).
 - [7] J. Brooke, D. Bitko, T. F. Rosenbaum, and G. Aeppli, Quantum Annealing of a Disordered Magnet, *Science* **284**, 779 (1999).
 - [8] G. E. Santoro, R. Martonak, E. Tosatti, and R. Car, Theory of Quantum Annealing of an Ising Spin Glass,

- Science **295**, 2427 (2002).
- [9] S. F. Edwards and P. W. Anderson, Theory of spin glasses, *J. Phys. F: Met. Phys.* **5**, 965 (1975).
 - [10] F. Barahona, On the computational complexity of Ising spin glass models, *J. Phys. A: Math. Gen.* **15**, 3241 (1982).
 - [11] M. W. Johnson et al., Quantum annealing with manufactured spins, *Nature* **473**, 194 (2011).
 - [12] R. Harris et al., Phase transitions in a programmable quantum spin glass simulator, *Science* **361**, 162 (2018).
 - [13] P. Weinberg, M. Tylutki, J. Rönkkö, J. Westerholm, J. A. Åström, P. Manninen, P. Törmä and A. W. Sandvik, Scaling and Diabatic Effects in Quantum Annealing with a D-Wave Device, *Phys. Rev. Lett.* **124** 090502 (2020).
 - [14] S. Zhou, D. Green, E. D. Dahl, and C. Chamon, Experimental realization of classical Z_2 spin liquids in a programmable quantum device, *Phys. Rev. B* **104**, L081107 (2021).
 - [15] A. D. King et al., Coherent quantum annealing in a programmable 2,000 qubit Ising chain, *Nat. Phys.* **18**, 1324 (2022).
 - [16] A. Ali, H. Xu, W. Bernoudy, A. Nocera, A. D. King, and A. Banerjee, Quantum Quench Dynamics of Geometrically Frustrated Ising Models, *Nature Comm.* **15**, 10756 (2024).
 - [17] A. D. King et al., Quantum critical dynamics in a 5000-qubit programmable spin glass, *Nature* **617**, 61 (2023).
 - [18] A. D. King et al., Beyond-classical computation in quantum simulation, *Science* **388**, 199 (2025).
 - [19] P. Sathe, A. D. King, S. M. Mniszewski, C. Coffrin, C. Nisoli, and F. Caravelli, Classical Criticality via Quantum Annealing, *arXiv:2505.13625*.
 - [20] T. I. Andersen et al., Thermalization and Criticality on an Analog-Digital Quantum Simulator, *arXiv:2405.17385*.
 - [21] A. Keesling, A. Omran, H. Levine, H. Bernien, H. Pichler, S. Choi, R. Samajdar, S. Schwartz, P. Silvi, S. Sachdev, P. Zoller, M. Endres, M. Greiner, V. Vuletić, and M. D. Lukin, Quantum Kibble–Zurek mechanism and critical dynamics on a programmable Rydberg simulator, *Nature* **568**, 207 (2019).
 - [22] P. Scholl et al., Programmable quantum simulation of 2D antiferromagnets with hundreds of Rydberg atoms, *Nature* **595**, 233 (2020).
 - [23] S. Ebadi et al., Quantum optimization of maximum independent set using Rydberg atom arrays, *Science*, eabo6587 (2022).
 - [24] T. Manovitz et al., Quantum coarsening and collective dynamics on a programmable simulator, *Nature* **638**, 86 (2025).
 - [25] T. Zhang, Observation of Near-Critical Kibble-Zurek Scaling in Rydberg Atom Arrays, *arXiv:2505.07930*.
 - [26] T. W. B. Kibble, *J. Phys. A* **9**, 1387 (1976).
 - [27] W. H. Zurek, *Nature (London)* **317**, 505 (1985).
 - [28] A. Polkovnikov, *Phys. Rev. B* **72**, 161201(R) (2005).
 - [29] W. H. Zurek, U. Dorner, and P. Zoller, Dynamics of a quantum phase transition, *Phys. Rev. Lett.* **95**, 105701 (2005).
 - [30] J. Dziarmaga, Dynamics of a quantum phase transition: Exact solution of the quantum Ising model, *Phys. Rev. Lett.* **95**, 245701 (2005).
 - [31] J. Dziarmaga, Dynamics of a quantum phase transition and relaxation to a steady state, *Adv. Phys.* **59**, 1063 (2010).
 - [32] A. Polkovnikov, K. Sengupta, A. Silva, and M. Vengalattore, Colloquium: Nonequilibrium dynamics of closed interacting quantum systems, *Rev. Mod. Phys.* **83**, 863 (2011).
 - [33] A. del Campo and W. H. Zurek, Universality of phase transition dynamics: Topological defects from symmetry breaking, *Int. J. Mod. Phys. A* **29**, 1430018 (2014).
 - [34] A. J. Bray, Theory of phase-ordering kinetics, *Adv. Phys.* **43**, 357 (1994).
 - [35] T. Blanchard, L. F. Cugliandolo, M. Picco and A. Tartaglia, Critical percolation in the dynamics of the 2d ferromagnetic Ising model, *J. Stat. Mech.* (2017) 113201.
 - [36] G. Biroli, L. F. Cugliandolo, and A. Sicillia, *Phys. Rev. E* **81**, 050101R (2010).
 - [37] A. Chandran, A. Erez, S. S. Gubser, and S. L. Sondhi, Kibble-Zurek problem: Universality and the scaling limit, *Phys. Rev. B* **86**, 064304 (2012).
 - [38] A. Chandran, F. J. Burnell, V. Khemani, and S. L. Sondhi, *J. Phys.: Cond. Mat.* **25**, 404214 (2013).
 - [39] A. Chandran, A. Nanduri, S. S. Gubser, and S. L. Sondhi *Phys. Rev. B* **88**, 024306 (2013).
 - [40] P. Gagel, P. P. Orth, and J. Schmalian, Universal postquench coarsening and aging at a quantum critical point, *Phys. Rev. B* **92**, 115121 (2015).
 - [41] R. Samajdar, D. A. Huse, Quantum and classical coarsening and their interplay with the Kibble-Zurek mechanism, *arXiv:2401.15144*.
 - [42] A. Pelissetto and E. Vicari, Dynamic Off-Equilibrium Transition in Systems Slowly Driven across Thermal First-Order Phase Transitions, *Phys. Rev. Lett.* **118**, 030602 (2017).
 - [43] F. Suzuki and W. H. Zurek, Topological Defect Formation in a Phase Transition with Tunable Order, *Phys. Rev. Lett.* **132**, 241601 (2024).
 - [44] J. Gao, Y. Lee, Y. Lim, D. Bae, T. Rabga, and Y. Shin, Universal Early Coarsening of Quenched Bose Gases, *Phys. Rev. Lett.* **128**, 135701 (2022).
 - [45] M. Schmitt, M. M. Rams, J. Dziarmaga, M. Heyl, and W. Zurek, Quantum phase transition dynamics in the two-dimensional transverse-field Ising model, *Sci. Adv.* **8**, eabl6850 (2022).
 - [46] J. Tindall, A. Mello, M. Fishman, M. Stoudenmire, and D. Sels, Dynamics of disordered quantum systems with two- and three-dimensional tensor networks, *arXiv:2503.05693*.
 - [47] L. Mauron and G. Carleo, Challenging the Quantum Advantage Frontier with Large-Scale Classical Simulations of Annealing Dynamics, *arXiv:2503.08247*.
 - [48] F. Zhong and Z. Xu, Dynamic Monte Carlo renormalization group determination of critical exponents with linearly changing temperature, *Phys. Rev. B* **71**, 132402 (2005).
 - [49] C. De Grandi, V. Gritsev, and A. Polkovnikov, *Phys. Rev. B* **81**, 012303 (2010).
 - [50] C. De Grandi, A. Polkovnikov, and A. W. Sandvik, *Phys. Rev. B* **84**, 224303 (2011).
 - [51] C. D. Grandi, A. Polkovnikov, and A. W. Sandvik, *J. Phys.: Cond. Mat.* **25**, 404216 (2013).
 - [52] C.-W. Liu, A. Polkovnikov, and A. W. Sandvik, *Phys. Rev. B* **89**, 054307 (2014).
 - [53] C.-W. Liu, A. Polkovnikov, and A. W. Sandvik, *Phys. Rev. B* **89**, 054307 (2014).

- [54] C.-W. Liu, A. Polkovnikov, and A. W. Sandvik, *Phys. Rev. Lett.* **114**, 147203 (2015).
- [55] S. J. Rubin, N. Xu, and A. W. Sandvik, *Phys. Rev. E* **95**, 052133 (2017).
- [56] N. Xu, K.-H. Wu, S. J. Rubin, Y.-J. Kao, A. W. Sandvik, *Phys. Rev. E* **96**, 052102 (2017).
- [57] N. Xu, C. Castelnovo, R. G. Melko, C. Chamon and A. W. Sandvik, *Phys. Rev. B* **97**, 024432 (2018).
- [58] M. P. Nightingale and H. W. J. Blöte, Monte Carlo computation of correlation times of independent relaxation modes at criticality, *Phys. Rev. B* **62**, 1089 (2000).
- [59] V. Spirin, P. L. Krapivsky, and S. Redner, Fate of zero-temperature Ising ferromagnets, *Phys. Rev. E* **63**, 036118 (2001).
- [60] V. Spirin, P. L. Krapivsky, and S. Redner, Freezing in Ising ferromagnets, *Phys. Rev. E* **65**, 016119 (2001).
- [61] K. Barros, P. L. Krapivsky, and S. Redner, Freezing into stripe states in two-dimensional ferromagnets and crossing probabilities in critical percolation, *Phys. Rev. E* **80**, 040101(R) (2009).
- [62] J. Olejarz, P. L. Krapivsky, and S. Redner, Fate of 2D Kinetic Ferromagnets and Critical Percolation Crossing Probabilities, *Phys. Rev. Lett.* **109**, 195702 (2012).
- [63] A. Lipowski, Anomalous phase-ordering kinetics in the Ising model, *Physica A* **268**, 6 (1999).
- [64] M. Plischke, Z. Rácz, and D. Liu, Time-reversal invariance and universality of two-dimensional growth models, *Phys. Rev. B* **35**, 3485 (1987).
- [65] K. Shimizu, Y. Kuno, T. Hirano, and I. Ichinose, Dynamics of a quantum phase transition in the Bose-Hubbard model: Kibble-Zurek mechanism and beyond, *Phys. Rev. A* **97**, 033626 (2018).
- [66] A. Libal, A. del Campo, C. Nisoli, C. Reichhardt, and C. Reichhardt, Quenched Dynamics of Artificial Spin Ice: Coarsening versus Kibble-Zurek, *Phys. Rev. Res.* **2**, 033433 (2020).
- [67] D. R. Mitchell, C. Adami, W. Lue, and C. P. Williams, Random matrix model of adiabatic quantum computing, *Phys. Rev. A* **71**, 052324 (2005).
- [68] T. Caneva, R. Fazio, and G. E. Santoro, Adiabatic quantum dynamics of the Lipkin-Meshkov-Glick model, *Phys. Rev. B* **78**, 104426 (2008).
- [69] T. Zanca and G. E. Santoro, Quantum annealing speedup over simulated annealing on random Ising chains, *Phys. Rev. B* **93**, 224431 (2016).
- [70] M. M. Wauters, R. Fazio, H. Nishimori, and G. E. Santoro *Phys. Rev. A* **96**, 022326 (2017).
- [71] H.-B. Zeng, C.-Y. Xia, and A. del Campo, Universal Breakdown of Kibble-Zurek Scaling in Fast Quenches across a Phase Transition, *Phys. Rev. Lett.* **130**, 060402 (2023).
- [72] A. Grabarits, F. Balducci, and A. del Campo, Driving a quantum phase transition at an arbitrary rate: Exact solution of the transverse-field Ising model, *Phys. Rev. A* **111**, 042207 (2025).
- [73] R. H. Swendsen and J.-S. Wang, Nonuniversal critical dynamics in Monte Carlo simulations, *Phys. Rev. Lett.* **58**, 86 (1987).
- [74] D. Aasen, R. S. K. Mong, and P. Fendley, Topological Defects on the Lattice I: The Ising model, *J. Phys. A: Math. Theor.* **49** 354001 (2016).
- [75] M. Hauru, G. Evenbly, W. W. Ho, D. Gaiotto, and G. Vidal, Topological conformal defects with tensor networks, *Phys. Rev. B* **94**, 115125 (2016).
- [76] J. Haegeman, J. I. Cirac, T. J. Osborne, I. Pižorn, H. Verschelde, and F. Verstraete, Time-dependent variational principle for quantum lattices, *Phys. Rev. Lett.* **107**, 1 (2011).
- [77] J. Haegeman, C. Lubich, I. Oseledets, B. Vandereycken, and F. Verstraete, Unifying time evolution and optimization with matrix product states, *Phys. Rev. B* **94**, 165116 (2016).
- [78] P. Czarnik, J. Dziarmaga, P. Corboz, Time evolution of an infinite projected entangled pair state: An efficient algorithm, *Phys. Rev. B* **99**, 035115 (2019).
- [79] M. Yang and S. R. White, Time-dependent variational principle with ancillary krylov subspace, *Phys. Rev. B* **102**, 094315 (2020).
- [80] J. Dziarmaga, Time evolution of an infinite projected entangled pair state: Neighborhood tensor update, *Phys. Rev. B* **104**, 094411 (2021).
- [81] J. Unfried, J. Hauschild, and F. Pollmann, Fast time evolution of matrix product states using the qr decomposition, *Phys. Rev. B* **107**, 155133 (2023).
- [82] J.-W. Li, A. Gleis, and J. Von Delft, Time-dependent variational principle with controlled bond expansion for matrix product states, *Phys. Rev. Lett.* **133**, 026401 (2024).
- [83] M. Schmitt, M. Heyl, Quantum many-body dynamics in two dimensions with artificial neural networks, *Phys. Rev. Lett.* **125**, 100503 (2020).
- [84] G. Carleo, F. Becca, M. Schiró, and M. Fabrizio, Localization and Glassy Dynamics Of Many-Body Quantum Systems, *Sci. Rep.* **2**, 243 (2012).
- [85] G. Carleo, F. Becca, L. Sanchez-Palencia, S. Sorella, and M. Fabrizio, Light-cone effect and supersonic correlations in one- and two-dimensional bosonic superfluids, *Phys. Rev. A* **89**, 031602(R) (2014).
- [86] B. Blaß and H. Rieger, Test of quantum thermalization in the two-dimensional transverse-field Ising model, *Sci. Reps.* **6**, 38185 (2016).
- [87] E. Hairer, S.P. Norsett and G. Wanner, "Solving ordinary Differential Equations I. Nonstiff Problems", 2nd edition. Springer Series in Computational Mathematics, Springer-Verlag (1993).
- [88] C. Hotta, T. Yoshida, and K. Harada, Quantum critical dynamics in the two-dimensional transverse Ising model, *Phys. Rev. Res.* **5**, 013186 (2023).
- [89] D. Poland, S. Rychkov, and A. Vichi, The conformal bootstrap: Theory, numerical techniques, and applications, *Rev. Mod. Phys.* **91**, 015002 (2019).
- [90] J. M. Deutsch, Eigenstate thermalization hypothesis, *Rep. Prog. Phys.* **81** 082001 (2018).
- [91] T. Banks and A. Lucas, Emergent entropy production and hydrodynamics in quantum many-body systems, *Phys. Rev. E* **99**, 022105 (2019).
- [92] M. Kolodrubetz, D. Pekker, B. K. Clark, and K. Sengupta, Nonequilibrium dynamics of bosonic Mott insulators in an electric field, *Phys. Rev. B* **85**, 100505(R) (2012).
- [93] A. Maraga, A. Chiochetta, A. Mitra, and A. Gambassi, Aging and coarsening in isolated quantum systems after a quench: Exact results for the quantum $O(N)$ model with $N \rightarrow \infty$, *Phys. Rev. E* **92**, 042151 (2015).
- [94] A. Maraga, P. Smacchia, and A. Silva, Linear ramps of the mass in the $O(N)$ model: Dynamical transition and quantum noise of excitations, *Phys. Rev. B* **94**, 245122 (2016).

- [95] B. Altshuler, H. Krovi, and J. Roland, Anderson localization makes adiabatic quantum optimization fail, *Proc. Nat. Acad. Sci.* **107** 12446 (2010).
- [96] M. Rigol, V. Dunjko, and M. Olshanii, Thermalization and its mechanism for generic isolated quantum systems, *Nature* **452**, 854 (2008).
- [97] R. Mondaini, K. R. Fratus, M. Srednicki, and M Rigol, Eigenstate thermalization in the two-dimensional transverse field Ising model, *Phys. Rev. E* **93**, 032104 (2016).
- [98] R. Mondaini and M. Rigol, Eigenstate thermalization in the two-dimensional transverse field Ising model. II. Off-diagonal matrix elements of observables, *Phys. Rev. E* **96**, 012157 (2017).
- [99] A. Dutta, A. Rahmani, and A. del Campo, Anti-Kibble-Zurek Behavior in Crossing the Quantum Critical Point of a Thermally Isolated System Driven by a Noisy Control Field, *Phys. Rev. Lett.* **117**, 080402 (2016).
- [100] Y. Bando and H. Nishimori, Simulated quantum annealing as a simulator of nonequilibrium quantum dynamics, *Phys. Rev. A* **104**, 022607 (2021).
- [101] Comment on: "Dynamics of disordered quantum systems with two- and three-dimensional tensor networks" arXiv:2503.05693, A. D. King et al., arXiv:2504.06283.
- [102] P. Weinberg and M. Bukov, *SciPost Phys.* **2**, 003 (2017), QuSpin: a Python package for dynamics and exact diagonalisation of quantum many body systems part I: spin chains, *SciPost Phys.* **7**, 020 (2019).